Interaction of steady jets with an array of permeable screens

Mustafa N. Musta · Paul S. Krueger

Abstract Turbulent flows in porous media have important practical applications such as enhanced mixing of fuel and air, food drying, and cooling of electronics. However, experimental studies of turbulence in porous media are sparse due to the difficulties of measuring the complex flow environment. To this end, the interactions of steady jets with a porous medium formed from several parallel, transparent, permeable screens are studied using digital particle image velocimetry in a refractive indexed-matched environment. The permeable screens had porosities (open area ratios, ϕ) of 83.8, 69.0, 55.7, and 49.5 % and were held by a transparent frame that allowed the screen spacing to be changed. The steady jet results for Reynolds number (Re), which is defined based on the jet exit velocity and jet diameter, of 1000 showed laminar, predominantly steady flow that was segregated inside the porous medium, but for $Re \geq 2000$, the flow was unsteady and turbulent with a mean velocity field that was relatively smooth inside the porous medium. As a result, more traditional jet features of self-similarity and increasing jet width were compared for the $Re \geq 2000$ results. Decreasing the porosity was observed to increase the width of the jet significantly, especially for low porosity screens, and slowed the jet flow speed. Some of the typical features for axisymmetric jets were observed, even though the flow impinged on the permeable screens. In particular, self-similarity (or near self-similar behavior) was observed for the cross-sectional mean velocity profiles and for turbulence quantities for porosities larger than 55.7 % inside the porous medium. The effect of ϕ on turbulence quantities was significant for $Re \geq 2000$. Although turbulence intensity increased on the downstream side of the first screen, the high dissipation forced drastic decrease of turbulence levels further downstream in the porous domain. Finally, the screens increased the removal of momentum from the jet as porosity decreased and screen spacing had a significant effect on the removal rate.

1 Introduction and background

Steady jets impinging on porous media have been used in many important natural and technological applications. For instance, in combustion technology, porous media burners have been proposed for use in liquid fuel combustors to enhance the rate of fuel mixing and reduce emission of pollutants (Jugjai et al. 2002; Shahangian and Ghojel 2010). Porous media can also be used in internal combustion engines to achieve homogenous mixing of gas and liquid (spray) flow to increase ignitability in diesel engines, which will lead to a decrease in NOx emissions (Jugjai et al. 2002).

Another application is in chemical and food engineering. Jets can be useful in drying of food and ingredients (Moreira 2001; Kudra and Mujumdar 2009), in which case large masses of food product (e.g., potato chips) can be represented as a porous medium. Other potential applications include vertical takeoff and landing of aircraft near forests or buildings, in which case the propulsive jet flow is subjected to complex and/or porous surfaces.

Due to the wide range of industrial applications and the complexity of the flow interactions, there have been several numerical studies of jets impinging on porous

M. N. Musta
Department of Aeronautical Engineering, Necmettin Erbakan University, Konya, Turkey
e-mail: mnmusta@konya.edu.tr

P. S. Krueger (✉)
Department of Mechanical Engineering, Southern Methodist University, Dallas, TX, USA
e-mail: pkrueger@lyle.smu.edu

media. Most of these investigations focus on convective heat transfer (e.g., Fu and Huang 1997; Jeng and Tzeng 2005; among others) and turbulent flows inside the porous media (Prakash et al. 2001b; Graminho and De Lemos 2009; among others). However, experiments are limited due to the difficulties in experimentation, which are mostly related to complexity and opaqueness of typical porous structures. Impinging jet flows are typically in the turbulent regime, so understanding the flow in porous media and validation of existing numerical tools in this flow regime are crucial for further enhancement of practical applications. Some experimentally guided numerical work has been done by Prakash et al. (2001a, b). Due to the difficulties stated above, experiments were done only in the clear fluid. From this work, it was concluded that in order to validate turbulence models in porous media, further experimental measurements inside the porous media are required.

Some experimental work has investigated steady turbulent jets impinging on a thin porous screen. Cant et al. (2002) considered a plane jet impinging on a single, thin (0.9 mm thick) porous screen with open area ratios $\phi = 41$–65 % and a solid wall with a jet Reynolds number of $Re \cong 15{,}000$ using laser doppler velocimetry (LDV) to measure flow on the upstream and downstream side of the screens. It was observed that for $\phi > 50$ %, the jet width increased with decreasing ϕ and the change in the jet width with ϕ was larger near the screen than further downstream. The centerline velocity decay downstream of the screens increased as the porosity decreased. Moreover, the decay of momentum and the axial volume flux were also dependent on the porosity of the screens and increased as the porosity decreased. Measurements of the transverse variation of the velocity profiles showed wall jets near the upstream side of the screens for low porosity ($\phi < 0.57$). Interestingly, the wall jets also appeared on the downstream side of the screens. The strength of the wall jets was dependent on ϕ and was stronger as ϕ decreased.

The second experimental study of a turbulent jet impinging on a single thin screen was by Webb and Castro (2006). They considered self-similar axisymmetric jets with Reynolds number greater than 23,000 impinging on a thin porous screen. The screen was placed at a downstream location of $x/D = 50$, and screens with open area ratios in the range $\phi = 22.6$–54 % were considered. Webb and Castro (2006) observed wall jets form upstream of the screen for $\phi < 40$ %, but no wall jets and no circulatory regions on the downstream side of the screen were observed, which was different from the plane jet study of Cant et al. (2002). It was also observed that as the porosity decreased, the centerline velocity downstream of the screen decreased more rapidly. Further downstream the velocity decay followed a constant decay rate. Although the jet half-width rapidly

increased for $\phi > 31.3$ % with a more rapid increase with ϕ for low ϕ values, the change of the half-width did not show a consistent trend with respect to ϕ further downstream. Momentum flux, axial volume flux, and axial turbulence fluctuations became very low as porosity decreased and showed nearly constant values downstream of the screen. At lower porosity ($\phi < 44.8$ %), the locations of the peak velocity in the cross-sectional velocity profiles was shifted from the center and turbulence levels downstream of the screen virtually collapsed to self-similar behavior.

Although the studies by Cant et al. (2002) and Webb and Castro (2006) provide important information about jet impingement on thin screens, they did not address the case of axially distributed porosity (e.g., multiple screens), which is important for investigating flow evolution inside a porous domain. Moreover, the measurements of the velocity field distribution, especially data near the screens, were sparse due to the limitations of the optical configuration used.

The objective of this study is to identify the effect of multiple permeable screens on the evolution of steady round jets in terms of the main flow kinematics, turbulence quantities, and kinetic energy. Although the effect of a single porous layer has been studied before in the self-similar regime, in real applications, the boundary complexity can be much higher and it is important to know the turbulence characteristics and flow regimes inside a distributed porous medium. Additionally, many applications do not utilize jet flows in the self-similar regime. The present study seeks to provide full flow field data inside the porous medium, which can be important not only for revealing the internal flow physics, but also for providing baseline behavior for validating computational models of turbulent flows in distributed porous media.

2 Experimental setup

A schematic of the experimental setup is shown in Fig. 1. The apparatus consisted of a glass tank containing an aqueous solution of glycerin, a cylindrical nozzle for generating steady jets, a pressurized tank for driving the flow, a frame for holding multiple permeable screens, a CCD camera, and a laser for flow illumination. It should be noted that this was the same setup used for vortex ring experiments (with the piston inside the tube removed to allow for long duration jets) (Musta and Krueger 2014), although only results after the jet had been on long enough to exhibit steady flow behavior are considered in the present investigation. The cylindrical nozzle had an inner diameter of $D = 37.33 \pm 0.25$ mm and wedge angle of $\alpha = 7°$ on the outer surface of the cylinder at the nozzle exit. The nozzle center line was 16.5 cm from the side walls of the tank and
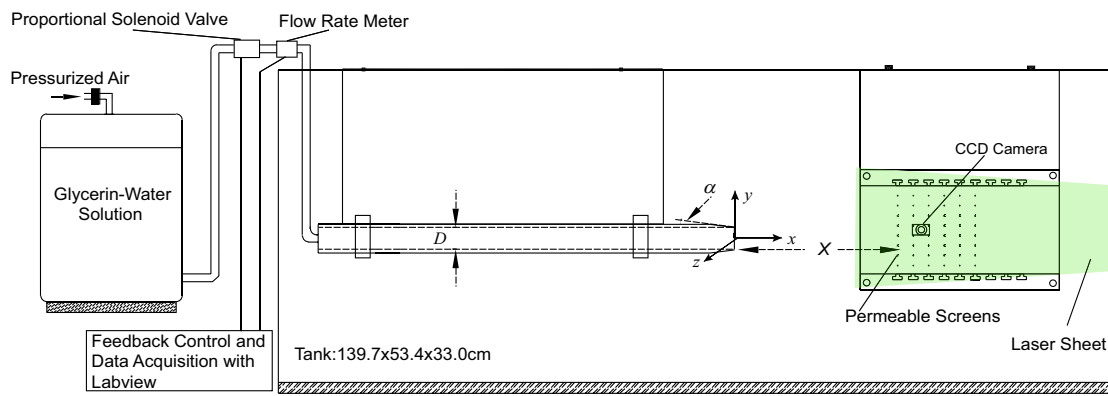
(a) Side View
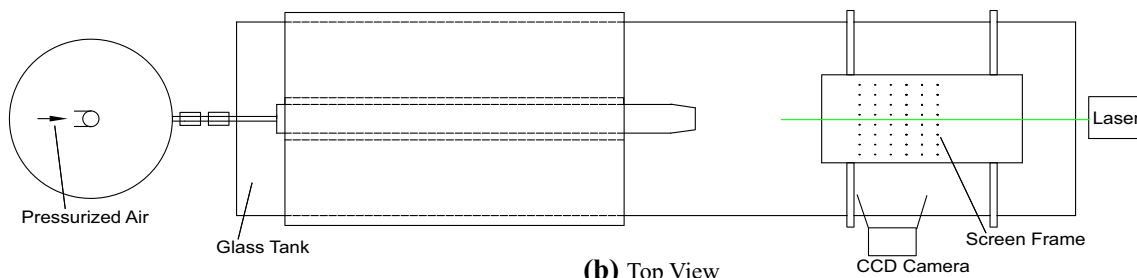
(b) Top View

Fig. 1 Schematic of experimental setup

25.78 cm below the liquid surface. The screen frame was 8.87 cm away from the back of the glass tank and 21.0 cm downstream of the nozzle exit plane.

The flow was driven through the cylindrical nozzle by the pressurized tank using air pressures of 0.16–0.21 MPa, depending on the Reynolds number of the experiments. Feedback control of the proportional solenoid valve (ASCO, Model SD8202G57V) via a computer and inline flow rate meter (Transonic Systems, Sensor Model ME 19 PX, flow meter Model TS410) allowed precise control of the jet velocity, U_{jet}. Jet Reynolds number was defined as $Re = \frac{U_{jet} D}{\nu}$, where ν is the kinematic viscosity of the aqueous solution of glycerin. Re was controlled to within 10 % of specified values with this setup.

The flow issuing from the tube impinged on an array of screens held downstream of the nozzle exit plane by a rigid transparent frame (Fig. 1a). The distance from the jet exit plane to the first screen (X) was kept constant, namely $X/D = 7.1 \pm 0.1$. This distance was chosen so that the steady jets were out of the potential core region before impinging on the first screen, which occurs for $X/D \geq 6$ for high Reynolds number test cases. At $x/D = 7$, the jets were not in the fully self-similar regime. Larger x/D ranges were not possible due primarily to the need to use refractive index-matched fluid for the experiments (described below). This is not viewed as a limitation of the results

since practical applications of impinging jets are frequently not in the self-similar regime, and the present results for the flow in the screens are compared to the free jet results from the same facility. Nevertheless, X would likely have a minor influence on the results through differences in upstream development of the jet, but this was not investigated.

The front and back of the frame were open to allow flow to penetrate the system, and the sidewalls were constructed from polycarbonate. T-slots were machined into the top and bottom of the frame for holding up to nine interchangeable permeable screens (see Fig. 2). The internal opening of the frame was a square cross section with a height of $H = 15.0$ cm. The slot placement provided a minimum allowable distance of $e/D = 0.69$ between screen rods. By removing screens from slots, the e/D distance could be increased in multiples of 0.69.

The screens were made in-house by molding PDMS (polydimethylsiloxane) into a grid shape with a rod diameter of 3.18 ± 0.005 mm (Musta 2012). This diameter was chosen to have enough stiffness for the tests due to the low Young's modulus of elasticity (~1 MPa) for PDMS. The open area ratio of the screens (ϕ) is defined as the cross-sectional open area in the axial direction (A_P) divided by total area in the axial direction, $\phi = \left(\frac{A_P}{A}\right)$. Screens with open area ratios of 49.5 ± 0.23, 55.7 ± 0.27, 69.0 ± 0.32, and 83.8 ± 0.38 % were constructed. The corresponding

Fig. 2 Schematics of **a** the frame geometry (screen cross sections shown as *black dots* in this view) and **b** a permeable screen

(a)   (b)
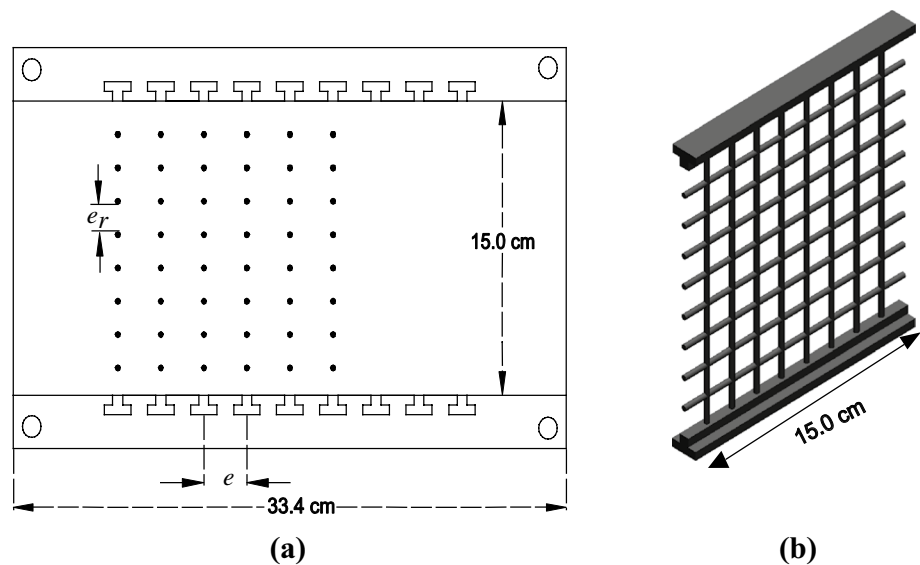
void ratios, $\frac{e_r}{D}$, for these screens were 18.89 ± 0.07, 25.69 ± 0.09, 37.08 ± 0.32, and 73.56 ± 0.27 %, where e_r is the distance between screen rods (see Fig. 2).

Full field measurement of the flow evolution using digital particle image velocimetry (DPIV) required optical access to the entire flow region. PDMS was chosen as the material for the permeable screens to facilitate optical access to the porous matrix since PDMS has a relatively low refractive index ($n \approx 1.41$) and because it could be molded into the desired shape. To match the refractive index of the fluid with that of the screens in order to eliminate illumination shadows in the measurement domain, an aqueous solution of glycerin [61 % (wt), glycerin supplied by US glycerin] was used as the working fluid. The resultant aqueous solution of glycerin had a measured kinematic viscosity of $8.9 \pm 0.1 \times 10^{-6}$ m^2/s, which is approximately seven times larger than the kinematic viscosity of water. This high viscosity limited the Reynolds numbers that were readily achievable.

The flow was illuminated with a frequency-doubled, pulsed Nd:YAG laser (200 mJ per pulse maximum, 532 nm wavelength) formed into a laser sheet of approximate thickness 1.5 mm that was aligned with nozzle center line. The flow field was imaged with a UNIQ UP-1830 CCD camera (1024 $\times$ 1024 pixel^2 resolution, 30 fps frame rate). Although the measurements were made with the refractive index of the fluid closely matched to the PDMS screens, slight variations in the refractive index and surface impurities (dust and/or small bubbles) on the screens caused unwanted light scattering from the surface of the screens. In order to minimize the effect of scattered light from the screens on the images and provide a clear optical field, the flow was seeded with 75–90 μm fluorescent particles and the flow was imaged using a high-pass filter to remove the laser light (Musta 2012). The particles were made in-house following a procedure similar to Pedocchi et al. (2008) and had an estimated density of 1.2 g/cm^3 (Pedocchi et al. 2008). The density of the working fluid was approximately 1.158 ± 0.005 g/cm^3, which was close enough to that of the particles to provide a long settling time for the particles.

Before processing the image data for velocity field information, the images were pre-processed using a digital image processing technique similar to Uzol et al. (2002) to eliminate image noise and any remaining scattered light that was not eliminated by analog filtering (Musta 2012). Following pre-processing, the images were processed for velocity data using 32 $\times$ 32 pixel^2 interrogation windows with 50 % overlap using a cross-correlation algorithm similar to that developed by Willert and Gharib (1991). A second processing pass utilized window-shifting (Westerweel et al. 1997) to reduce error and improve vector fields. Minor refractive index mismatches noted above had no significant impact on the accuracy of the results, including turbulence quantities, because the index of refraction was tuned to eliminate all visible shadows, making any optical disturbance much smaller than the interrogation window size. The contribution of particle displacement and particle size on the uncertainty of turbulence quantities was considered using the results of Wilson and Smith (2013). The uncertainty in the mean velocities was estimated as 2 %. For the fluctuating components, the uncertainty in $\frac{\langle u'u' \rangle}{U_{cl}^2}$ was estimated as 2.5 % and the uncertainty in $\frac{\langle u'v' \rangle}{U_{cl}^2}$ was estimated as 4 %.

Measurements were made for $Re = 1000$, 2000 and 3000 with open area ratios of $\phi = 100.0$, 83.8, 69.0, 55.7 and 49.5 % for three measurement regions to balance the field of view (FOV) and spatial resolution requirements of
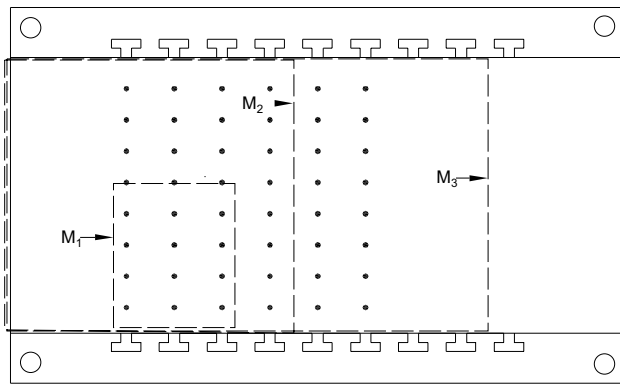
Fig. 3 Measurement domains

the investigation. Figure 3 shows the selected measurement domains. By increasing the camera magnification, feature resolution was increased at the expense of a smaller FOV.

The most common measurement domain was M_3 using six screens for $e/D = 0.69$ and four screens for $e/D = 1.38$. All the screen slots were not used for all the test cases. Increasing the number of the screens and decreasing the open area ratio increased the flow dissipation so that the majority of the flow had dissipated before the final screen slots. Measuring the flow in this region only served to decrease the measurement resolution. Measurements using the M_1 region were made for the open area ratios of 55.7 and 69.0 %, to get detailed, local information near the screens, and to measure the effect of the e_r/D on the flow evolution.

Measurements in the cross-plane (y–z plane) were made for $\phi = 55.7$ and 83.8 % at $e/D = 0.69$, and $Re = 3000$. For these measurements, experiments were made midway between screens 1–2, 2–3 and 3–4.

3 Qualitative flow field behavior

Experiments for $\phi = 100$ % were made to compare the interaction of the jet with the porous screens to the free jet case in the same facility. At $Re = 1000$, the $\phi = 100$ % instantaneous results showed laminar behavior with an occasional sinus-type variation in the flow, which was the first sign of instability (Crow and Champagne 1971). The dimensionless centerline velocity decay rate (slope of U_{jet}/U_{cl} vs x/D) was very low (approximately 2.5 %, see Fig. 12) which indicates laminar flow. These results are consistent with Todde et al. (2009) who showed that jets at $Re < 1600$ and $0 < x/D < 15$ exhibit laminar flow behavior. For $Re = 2000$, the instantaneous flow fields were unsteady. The (dimensionless) rate of centerline velocity decay for $Re = 2000$ was 25 % and large-scale structures developed in the flow field and spread radially to give a "wavy" motion to the jet flow. For $Re = 3000$, flow unsteadiness

and centerline velocity decay similar to the $Re = 2000$ case were observed. When combined with the turbulence intensity measurements (T_u) exceeding 20 % of the centerline velocity (see Sect. 5), these results for $Re = 2000$ and 3000 are indicative of turbulent flow behavior. Similar flow regimes were observed by Kwon and Seo (2005).

Effect of the porous medium on the jet is first illustrated qualitatively by considering instantaneous flow fields for the M_3 FOV. Figure 4 shows sequences of two instantaneous vector fields at $Re = 1000$ for $\phi = 83.7$ and 55.7 % with $e/D = 0.69$. The time for the corresponding frames in each sequence was normalized as $t^* = \frac{tU_{jet}}{D}$. For these cases, the flow is nearly steady (only small fluctuations are present) with the flow dividing sharply at locations where the jet impinges on the screen rods (the cross sections of the screen rods in the measurement plane are indicated by the black circles in the figures). For high ϕ, mild sinuous flow oscillations can be observed on the centerline, especially downstream of $x/D = 10.5$ (Fig. 4a–b). It is possible that this is due to the central jet-like flow becoming unstable downstream of the screen rods. The lower ϕ value shows nearly steady flow conditions with minimal flow oscillations downstream of the first screen. Any mild unsteadiness present could be associated with or induced by vortex-shedding behavior near the circular screen rods where the Re based on the rod diameter and upstream average velocity is $Re_d \sim 570$.

For higher Reynolds number, unsteady flow behavior dominates for all cases. Figure 5 shows instantaneous flow fields for $Re = 3000$ at $\phi = 83.8$ and 55.7 % with $e/D = 0.69$. The results for $Re = 2000$ are qualitatively similar (Musta 2012). For both ϕ, the upstream flow changes direction with time (the jet is "wagging"). This wagging behavior is not continuous through the screens and seems to attenuate as the flow moves downstream. Similar transition from steady to wagging behavior with increasing Reynolds number was observed by Kwon and Seo (2005) for the case of a free jet. For $\phi = 83.8$ %, dissipation is lower and the flow is split into three regions based on the screen geometry, with higher speed on the centerline. For $\phi = 55.7$ %, the jet is spread out and the downstream flow speed decreases to very low levels. A weak recirculation zone is generated upstream of the first screen for this case. To show the direction of velocity vectors and circulation regions, instantaneous streamlines are shown on the upstream side of the first screen (Fig. 5c–d).

Mean velocity field data for steady jets impinging on the permeable screens are presented in Figs. 6, 7, 8 and 9 for low- and high-resolution data at $Re = 1000$ and 3000. The mean velocity fields were obtained by averaging over 1000 vector fields for all cases.

The $Re = 1000$ data (Figs. 6, 7) show that decreasing ϕ causes the flow to split into multiple directions based on
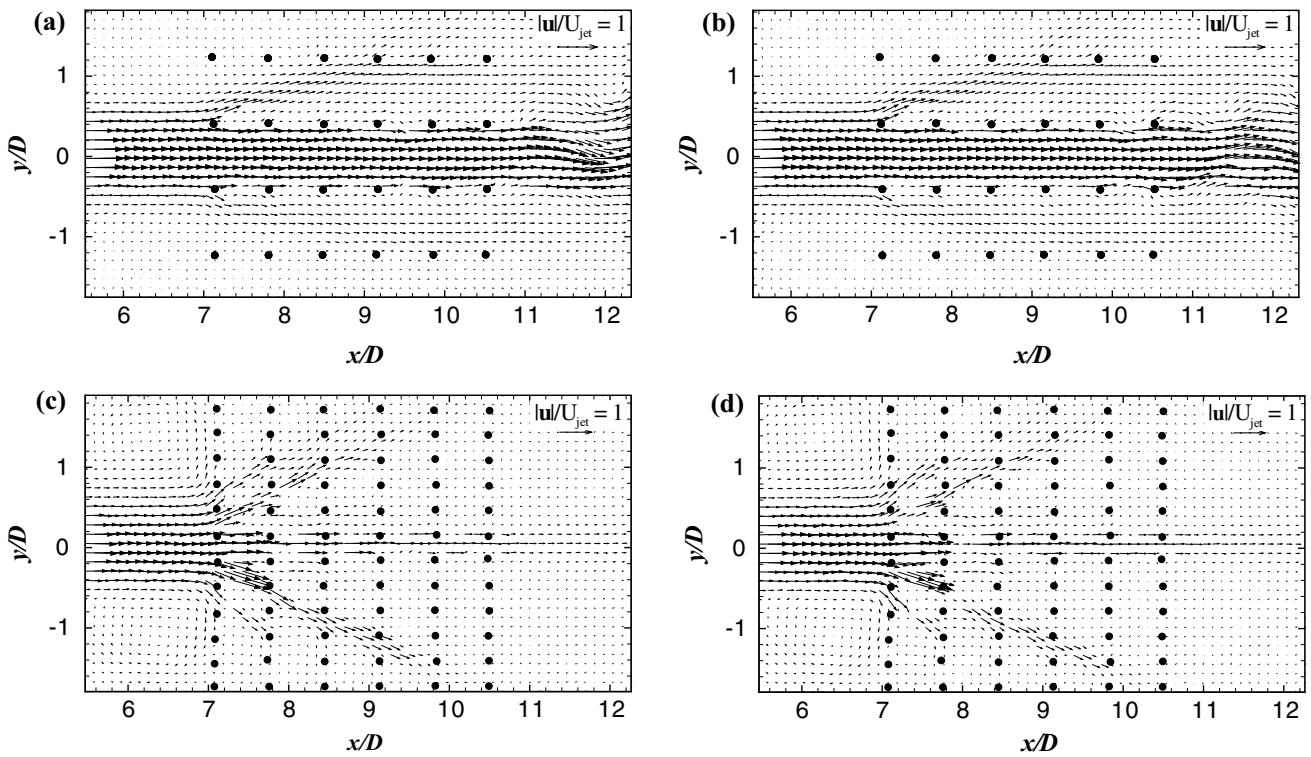
Fig. 4 Instantaneous flow fields for $Re = 1000$: **a** $t^* = 12.32$, $\phi = 83.8$ %; **b** $t^* = 12.94$, $\phi = 83.8$ %; **c** $t^* = 12.32$, $\phi = 55.7$ %; **d** $t^* = 12.94$, $\phi = 55.7$ %
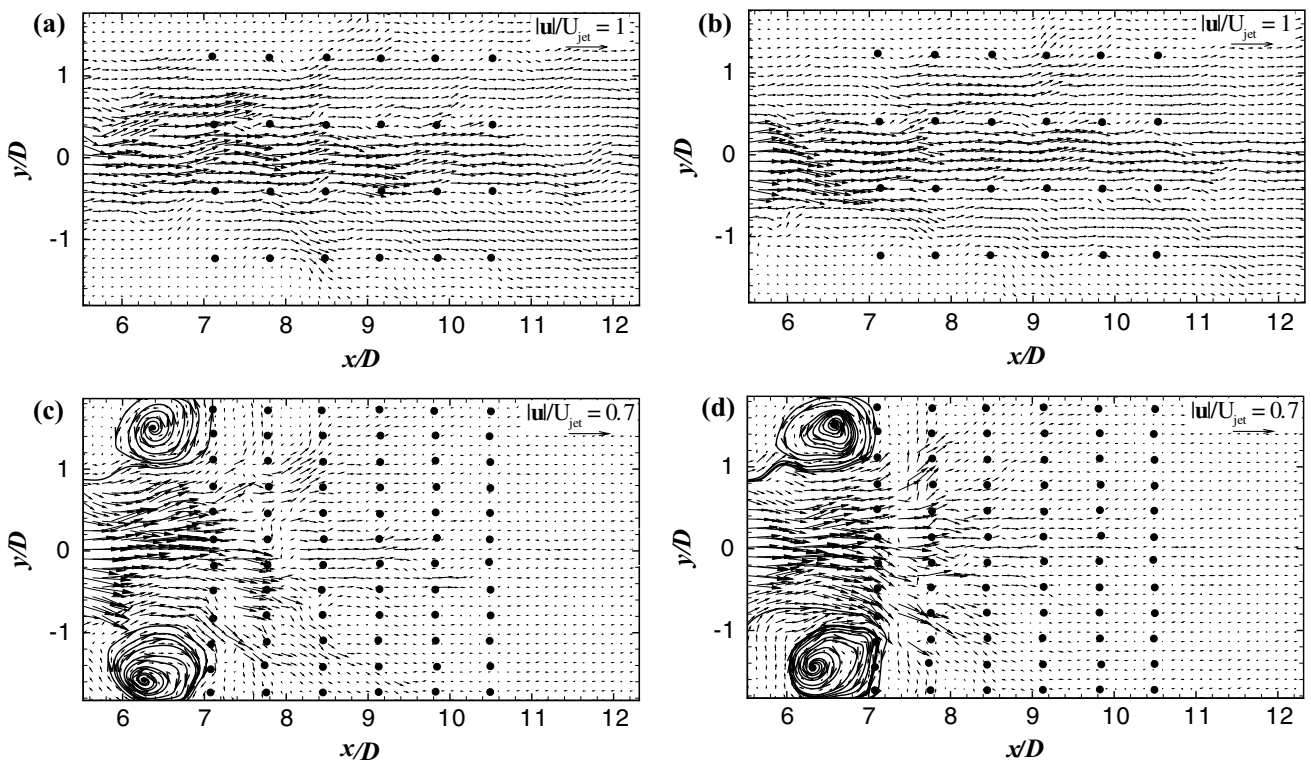

Fig. 5 Instantaneous flow fields for $Re = 3000$: **a** $t^* = 12.32$, $\phi = 83.8$ %; **b** $t^* = 12.94$, $\phi = 83.8$ %; **c** $t^* = 12.32$, $\phi = 55.7$ %; **d** $t^* = 12.94$, $\phi = 55.7$ %
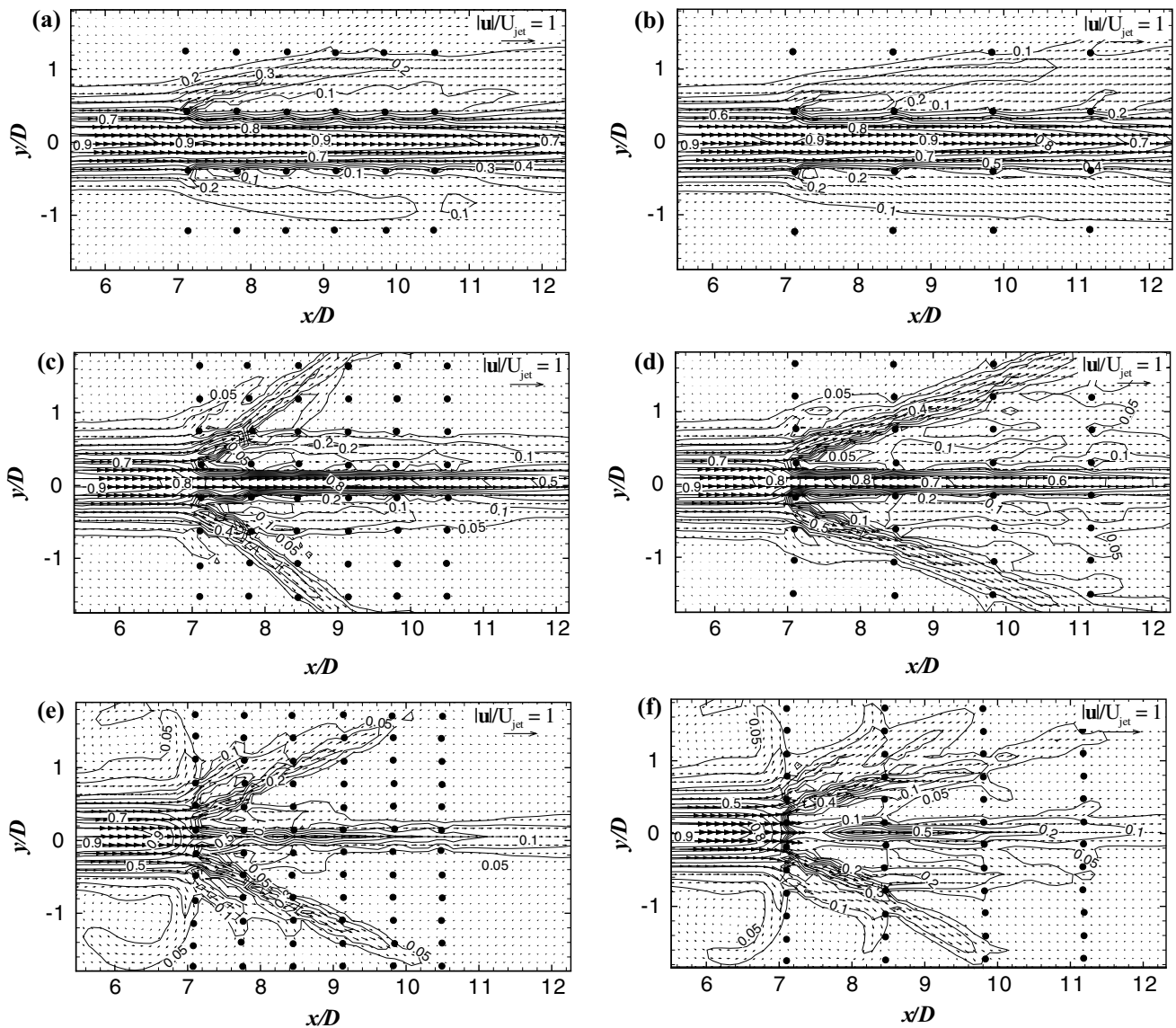
Fig. 6 Low-resolution (FOV = M_3) mean velocity fields at $Re = 1000$: **a** $\phi = 83.8$ %, $e/D = 0.69$; **b** $\phi = 83.8$ %, $e/D = 1.38$; **c** $\phi = 69.0$ %, $e/D = 0.69$; **d** $\phi = 69.0$ %, $e/D = 1.38$; **e** $\phi = 55.7$ %, $e/D = 0.69$; and **f** $\phi = 55.7$ %, $e/D = 1.38$

the screen rod locations and large wakes are formed downstream of the screen rods. Jet-like flow structures form on the centerline based on the pore size of the screens and the rest of the jet diameter splits into multiple directions after impinging on the screens. This splitting is stable, with little to no variation in time at this Reynolds number. In effect, voids in the screens act like channels for the flow.

For $\phi = 83.8$ % ($Re = 1000$), due to the high open area ratio, radial spreading of the flow is the lowest and the axial reduction of the flow speed is small. The effect of e/D on the mean flow field for $\phi = 83.9$ % is not pronounced, with the main effect being a slight change in the deflection angle of the flow separation from the central stream (Fig. 6a–b). For $\phi = 69.0$ %, the flow spreads at a larger angle with

decreasing e/D. The part of the jet separated from the central stream impinges on the frame wall near $x/D = 9$ for $e/D = 0.69$ and $x/D = 11$ for $e/D = 1.38$ (Fig. 6c–d). The $\phi = 55.7$ % results illustrate a weak recirculation zone upstream of the first screen in Fig. 6e–f. Radial flow features between screens 1–2 and 2–3 for $e/D = 0.69$, and between screens 1–2 for $e/D = 1.38$ appear as weak semi-circular features in the mean flow field. The radial flow is visible in these cases because of the strong blockage effect from the screens. Interaction with the frame wall causes the flow to wrap back around in the upstream direction. Similar flow structure was determined from the radial velocity profiles for $\phi = 23$–37 % by Webb and Castro (2006) as related to a wall jet upstream of single screens. In addition,
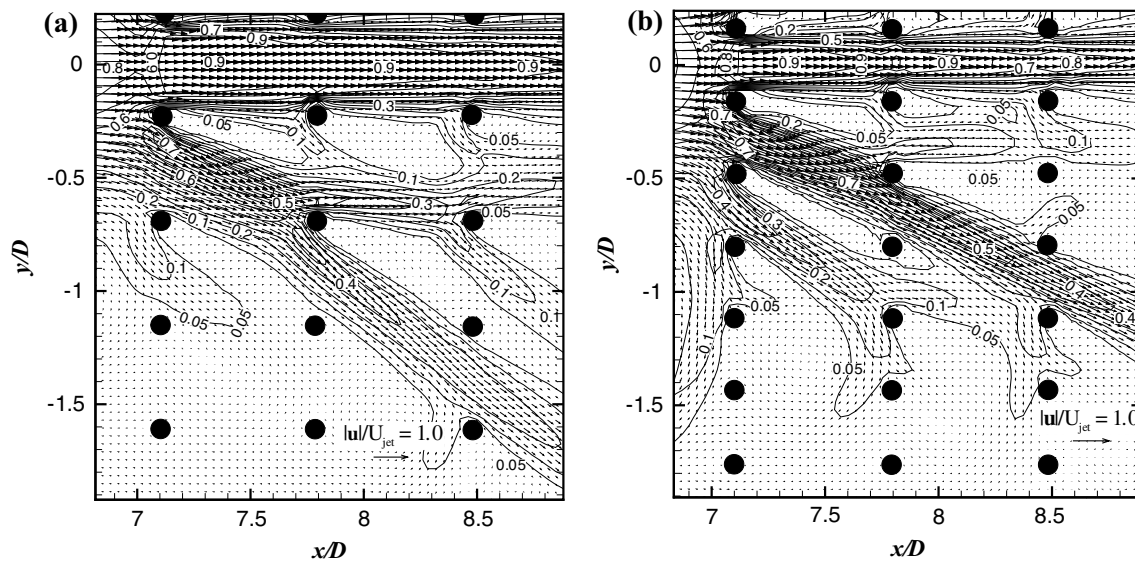
Fig. 7 High-resolution (FOV = M_1) mean velocity fields at $Re = 1000$: **a** $\phi = 69.0$ %, $e/D = 0.69$; and **b** $\phi = 55.7$ %, $e/D = 0.69$

Cant et al. (2002) concluded from the radial velocity profiles that wall jets existed both upstream and downstream of the screen and circulation upstream of the screen was observed for a planar jet impinging on the screen.

The high-resolution data (Fig. 7) more clearly illustrate the radial flow upstream of the first screen and between screens 1 and 2 for the $\phi = 55.7$ % case, which appear as weak circulation regions formed upstream of the first screen and semi-circular flow structures (flow starting to turn upstream) appear for large y/D. These structures become larger with increased e/D (not shown in Fig. 7). Very fine scale splitting of the jet flow is observed in the high-resolution results, indicating small adjustments (on the order of the screen rod diameter) to the screen rod locations (by adjusting ϕ or e/D) can have a significant effect on the overall flow structure.

Mean velocity profiles at $Re = 3000$ in Fig. 8 show that, unlike the $Re = 1000$ case, the jet does not split into discrete directions downstream of the first screen, but instead finger-type flow structures in the mean flow field form between the screen rods. Here, the "wagging" unsteady nature of the jet flow causes the time-averaged flow to fill out between screens, rather than follow discrete paths through the obstructions. The screens increase the jet spreading rate for all ϕ, with the majority of the effect occurring at the first screen. Associated with the in-filling between the screens, narrower wake regions (compared to $Re = 1000$) are observed downstream of the screen rods. Together with the increased jet spreading rate for decreased ϕ, the flow speed also decreases considerably for reduced ϕ due to increased dissipation. Although the instantaneous flow fields show unsteady behavior, the time-averaged flow fields are nearly symmetrical

with respect to the centerline of the jet. Recirculation regions appear upstream of the first screen for smaller ϕ and can be readily observed for the $\phi < 69$ % cases, similar to the $Re = 1000$ results. Downstream of the first screen, radial wall jets are apparent for $\phi < 69$ %, but complete recirculation regions are not apparent between screens 1 and 2 in Fig. 8.

The high-resolution data (Fig. 9) show the recirculation regions upstream of the screens more clearly, especially for the $\phi < 69.0$ % results. Additionally, the formation of a recirculation region between screens 1–2 for $\phi = 55.7$ % can be observed in Fig. 9b, where instantaneous streamlines are included to highlight the recirculation region. On the upstream side of the screens, the mean flow speed decreases as it approaches the screen plane, and then, it increases as it passes between screen rods, providing multiple jets downstream of the screen planes. The $e/D = 1.38$ results show similar behavior, but clear recirculation between screens 1–2 is not observed.

To further illustrate the overall flow symmetry and the three-dimensional shape of the flow structures identified in the previous results, measurements of the flow evolution were made in the cross-plane (y–z plane). Figure 10 shows mean velocity field measurements in the y–z plane at $x/D = 7.35$, 8.04 and 9.42 (midway between screens 1 and 2, 2 and 3, and 3 and 4, respectively) for $\phi = 83.6$ %, $e/D = 0.69$ and $\phi = 55.7$ %, $e/D = 0.69$ at $Re = 3000$. The vectors have been scaled according to U_{jet}. All results show high degree of symmetry between all locations and show the pore structure due to the very low velocity behind the screen rods. It should be noted that the degree of symmetry was sensitive to the relative location of the jet axis and center of the screens.
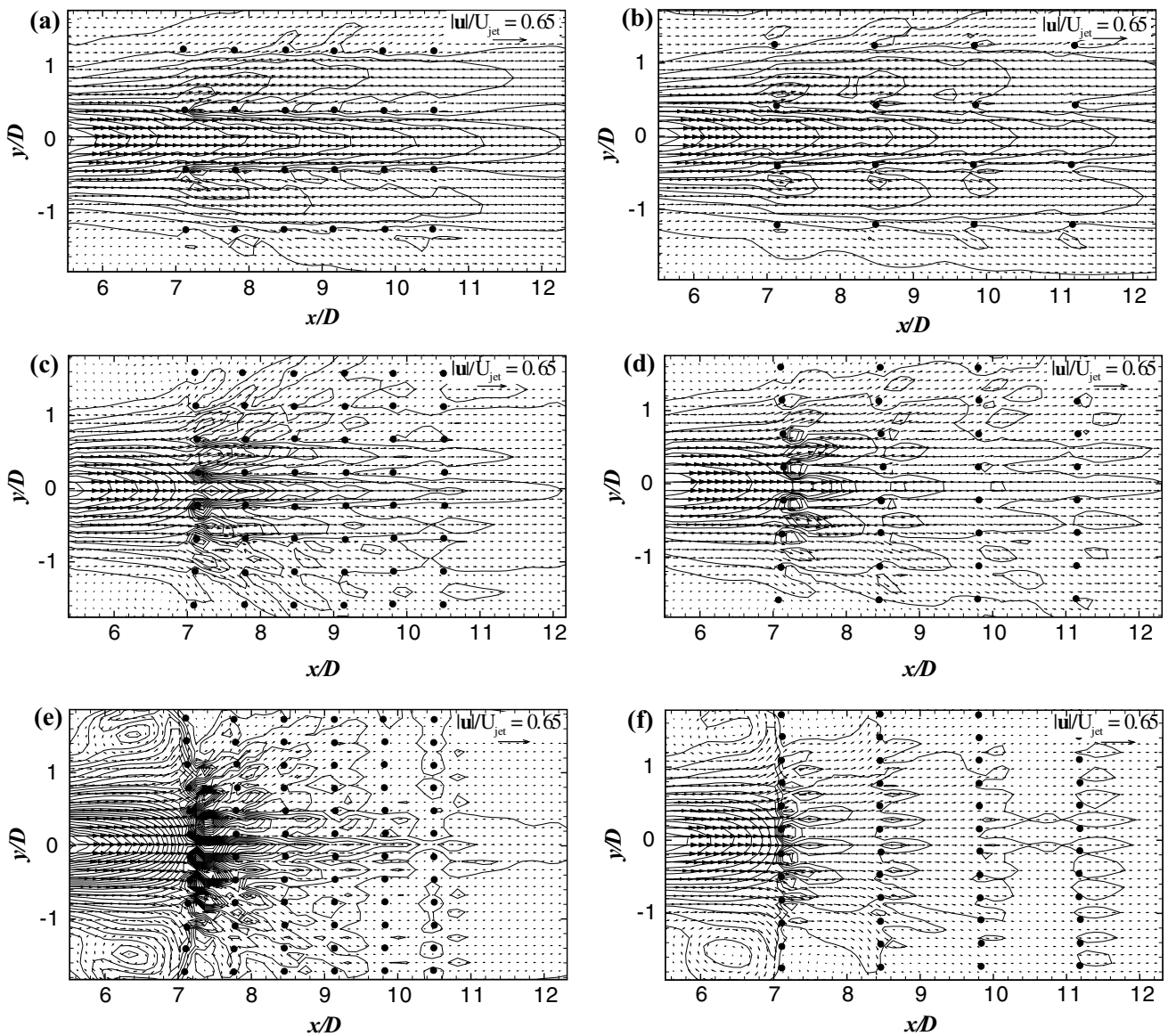
Fig. 8 Low-resolution (FOV $= M_3$) mean velocity fields at $Re = 3000$: **a** $\phi = 83.8$ %, $e/D = 0.69$; **b** $\phi = 83.8$ %, $e/D = 1.38$; **c** $\phi = 69.0$ %, $e/D = 0.69$; **d** $\phi = 69.0$ %, $e/D = 1.38$; **e** $\phi = 55.7$ %, $e/D = 0.69$; and **f** $\phi = 55.7$ %, $e/D = 1.38$

To obtain a more quantitative comparison of results for the different ϕ and Re cases, the following sections will discuss traditional measures of jet behavior, beginning with jet centerline velocity and half-width evolution.

4 Effect of ϕ on the jet centerline velocity and the jet half-width

Figure 11 shows the mean centerline velocity for all Reynolds numbers and all ϕ values. Vertical dashed lines show the screen x-axis locations for $e/D = 0.69$ and 1.38. Following common practice for free jet results, the mean

centerline velocity, U_{cl}, is plotted dimensionless as $\frac{U_{jet}}{U_{cl}}$ so that the decay is more easily observed as an increase in $\frac{1}{U_{cl}}$. Also, because the decay in U_{cl} is more rapid for the cases with screens, the results are plotted on a semi-log plot.

Overall, Fig. 11 shows that decreasing ϕ increases the jet velocity decay (decreases U_{cl}) and the decay appears to follow a linear trend with x/D (on average) on the semi-log plot (indicative of exponential increase in $1/U_{cl}$ with x/D) for $Re = 2000$ and 3000. For $Re = 1000$, the decay in U_{cl} also increases with decreasing ϕ, but the trend with x/D appears to have more of a parabolic behavior for low ϕ. For all Re, the $\phi = 83.8$ % cases show centerline velocity decay close in magnitude to the free jet results between
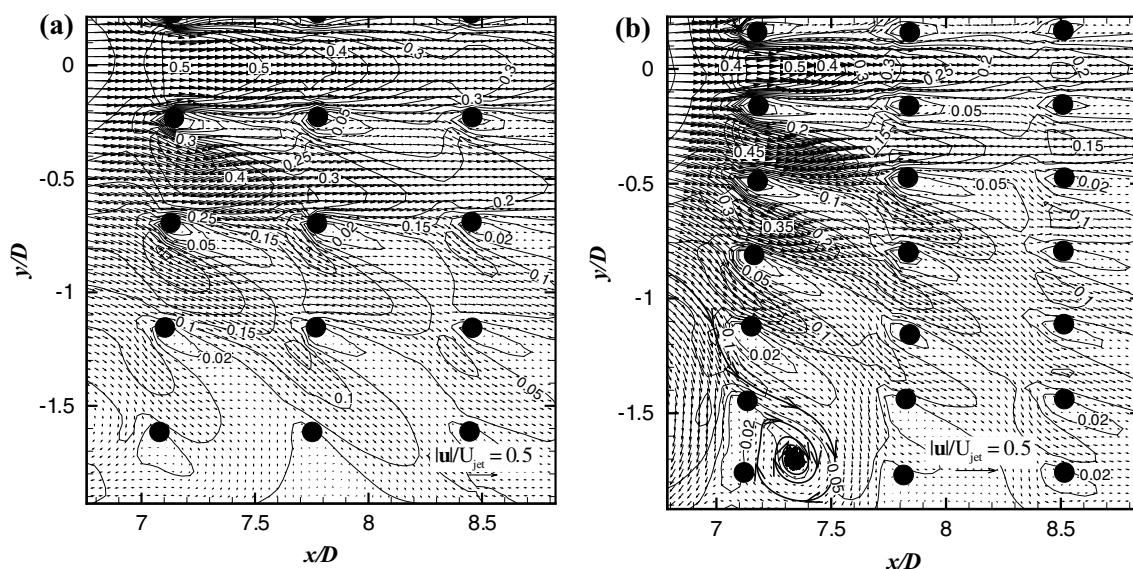
Fig. 9 High-resolution (FOV = M_1) mean velocity fields at $Re = 3000$: **a** $\phi = 69.0$ %, $e/D = 0.69$; and **b** $\phi = 55.7$ %, $e/D = 0.69$

$6 < x/D < 8.5$. Oscillations in the trends show the effect of the screens, which cause the centerline velocity to decay when approaching the screen and then increase as it passes through the screens due to the pressure change across the screens. The effect of changing e/D was limited for all the Re cases, and the effect of the Reynolds number on the decay was not as strong for the $Re = 2000$–3000 results compared to the $Re = 1000$ results.

Quantitative comparison of the overall trends was performed by determining the inverse slope K according to the equation

$$\frac{U_{\text{jet}}}{U_{\text{cl}}} = \frac{1}{K}\left(\frac{x}{D} - \frac{x_0}{D}\right) \tag{4.1}$$

where x_0 is a virtual origin for the observed trends. The velocity constant K indicates the rate of centerline velocity decay and is shown in Fig. 12 as a function of ϕ for all cases. The values of K and x_0 were determined using linear regression of the data downstream of the first screen. Error bars on the plot show the possible range of K based on the regression (accounting for nonlinearity in the data). The $\phi = 100$ % measurements can be compared with the free jet results in the literature, although in the present study there is an effect from the frame and the measurements were made in the intermediate region ($6 < x/D < 12$). For $Re = 2000$ and 3000, $K = 3.97$ and 4.37, respectively, for the present results at $\phi = 100$ %. In the literature, Todde et al. (2009) found $K = 4.64$ for $Re = 2164$–4000 at ~$11 < x/D < 40$ and Kwon and Seo (2005) found $K = 5.5$ for $Re = 1305$–5142 at $15 < x/D < 75$. The current values are somewhat smaller than these, but this difference is most likely due to the measurement location (notice that the

free jet results from literature show a slight decrease in K as the average measurement region moves closer to the jet exit plane) and the effect of the confinement. The smaller value for $Re = 2000$ is likely related to weak Re effects at these lower Re. The higher K values with screens for the $Re = 1000$, $\phi > 49.5$ % results is due to the slower decay of the centerline velocity in this case, which is expected since the flow near the core remains confined to this area without much lateral spreading or dissipation (see Fig. 4). Decreasing the open area ratio decreases K (increases the decay rate). For $Re = 2000$ and 3000, the trends in K are very similar and show a nearly exponential growth with ϕ over most of the ϕ range.

The jet half-width, b, is traditionally defined as the distance from the centerline to the location where the mean jet velocity reaches half of the centerline velocity. However, for the cases with permeable screens ($\phi < 100$ %), jet-like flow structures were formed between the screens. This produced highly irregular jet velocity profiles, and the traditional definition of the jet width was inadequate for such cases since the velocity profile was not monotonic [for the free jet results in the presence of the frame compared with traditional free jet results from the literature see Musta (2012)]. To avoid complications with the traditional definition, a generalized integral width was defined according to,

$$r_{1/e} = \frac{1}{2}\left[\frac{\int_0^{H/2} \langle u \rangle y\,\mathrm{d}y}{\int_0^{H/2} \langle u \rangle\,\mathrm{d}y} + \frac{\int_{-H/2}^{0} \langle u \rangle y\,\mathrm{d}y}{\int_{-H/2}^{0} \langle u \rangle\,\mathrm{d}y}\right] \tag{4.2}$$

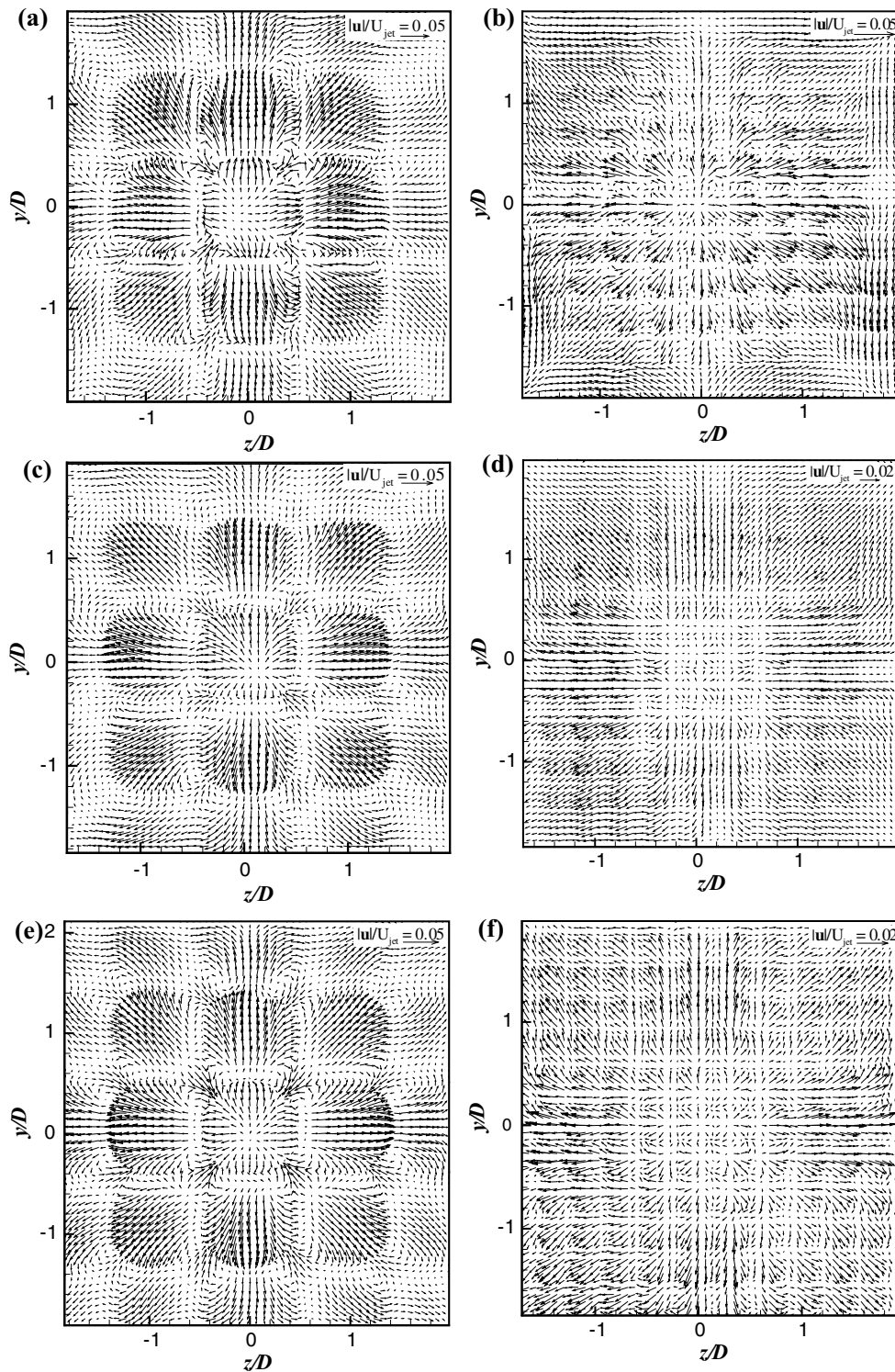where $y = 0$ is the centerline (i.e., the location of the maximum velocity in the cross section) and H is the frame

Fig. 10 Mean velocity fields in the y–z plane at $Re = 3000$ for $e/D = 0.69$: At $x/D = 7.35$ **a** $\phi = 83.6$ % and **b** $\phi = 55.7$ %; at $x/D = 8.04$: **c** $\phi = 83.6$ % and **d** $\phi = 55.7$ %; at $x/D = 8.73$: **e** $\phi = 83.6$ % and **f** $\phi = 55.7$ %

height defined in Sect. 2. Following the notation of Kwon and Seo (2005), $r_{1/e}$ represents the jet width, and the jet width for each cross section was calculated using Eq. 4.2.

The rate of change of $r_{1/e}$ with x is shown Fig. 13. The results for $Re = 1000$ are not presented in this figure since the jet split into the multiple pieces and formed a highly
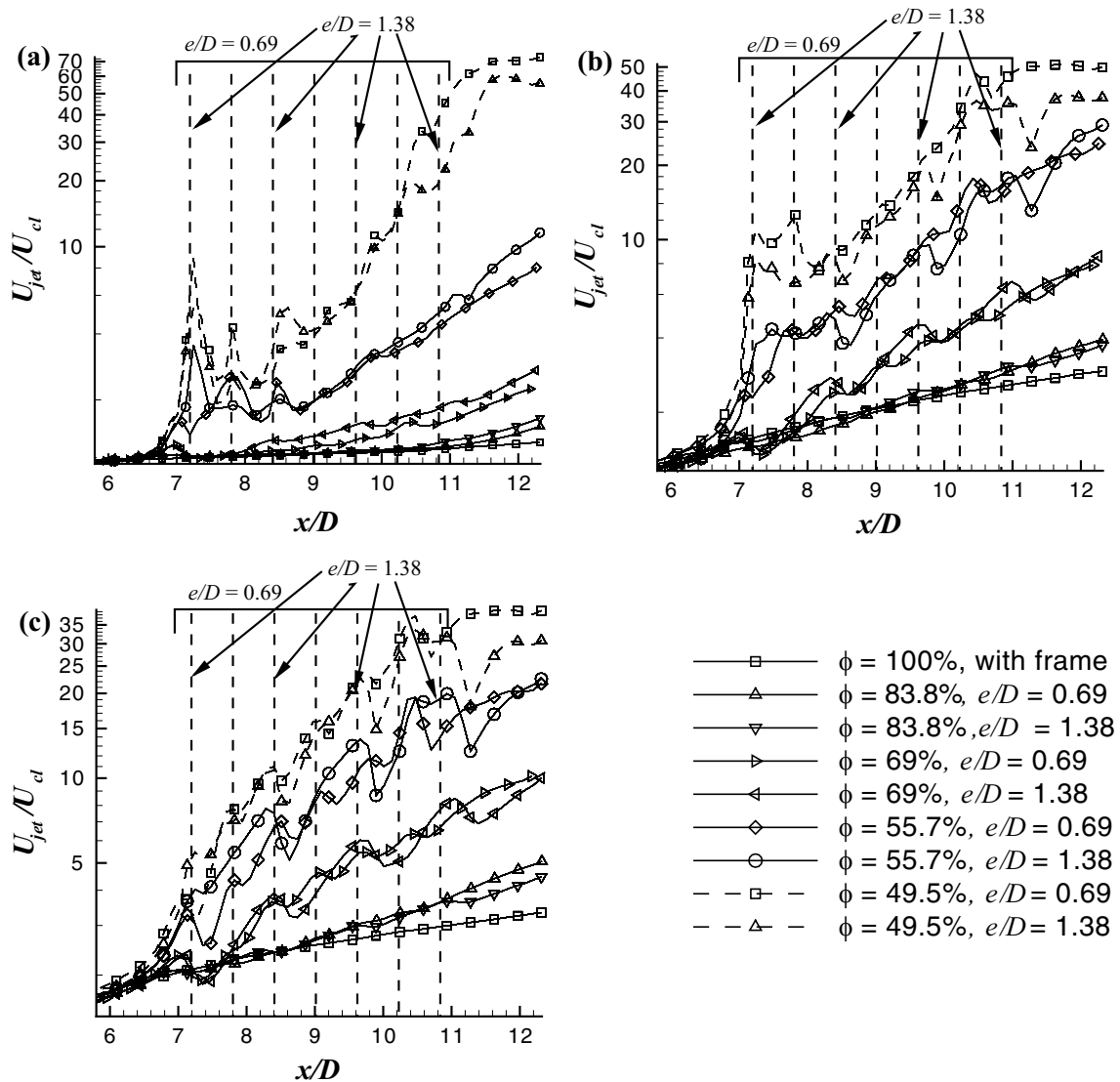
Fig. 11 Decay of mean centerline velocity for **a** $Re = 1000$; **b** $Re = 2000$; and **c** $Re = 3000$

segregated structure. The values were determined as the slope of a linear regression of $r_{1/e}$ from the first screen over the remainder of FOV for the low-resolution measurement domain, and error bars on the graph show the possible range of values based on regression. The $\phi = 100$ % results in Fig. 13 are lower than expected for a free jet, where traditionally $db/dx \sim 0.1$. Due to the integral definition of $r_{1/e}$, the value of $dr_{1/e}/dx$ is affected by the shape of the velocity profile and tends to be significantly smaller than values based on b, so the $dr_{1/e}/dx$ results for $\phi = 100$ % are also shown in Fig. 13 for comparison with the permeable screen results. For $\phi < 100$ %, the $Re = 2000$ and 3000 results shown here indicate that decreasing ϕ increases $dr_{1/e}/dx$ by separating the jet flow as it moves downstream. Increasing the Reynolds number decreases $dr_{1/e}/dx$ slightly and e/D

has little effect on this parameter for $Re = 3000$, but e/D does appear to affect the jet spreading rate at $Re = 2000$ for $\phi < 83.8$ %.

5 Cross-sectional profiles of jet flow quantities

Cross sections of the jet velocity profiles for the $Re = 2000$ case are shown in Fig. 14. The $Re = 1000$ and $Re = 3000$ results are not shown here since the segregated behavior of the $Re = 1000$ results does not follow typical jet behavior and the $Re = 2000$ results are qualitatively similar to the $Re = 3000$ results (Musta 2012). The mean velocity, $\langle u \rangle$, in Fig. 14 was obtained by averaging more than 1000 instantaneous velocity fields and normalizing by the local
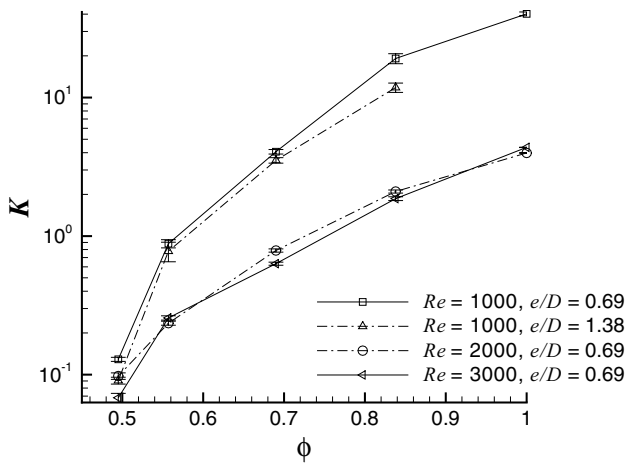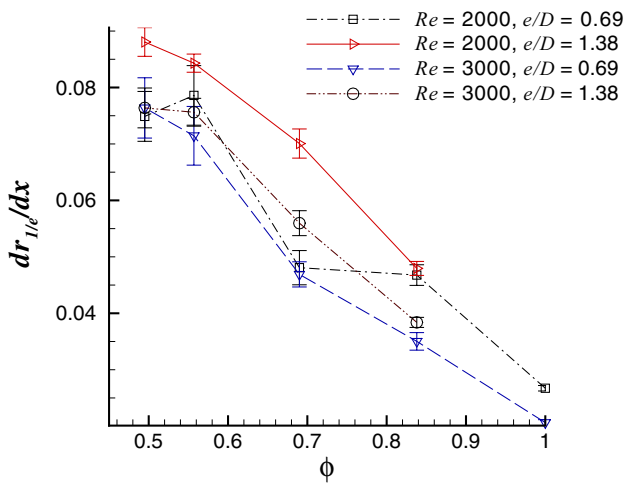
Fig. 12 Change of velocity constant K versus ϕ

Fig. 13 Rate of change of the jet width

maximum centerline velocity. For $\phi = 100$ %, the results (normalizing y by b in this case) show near self-similarity over the cross section, especially for $x/D > 7.35$ (Fig. 14a). The velocity profiles for cases with screens show that the flow is not completely self-similar, but the large ϕ ($\phi > 55.7$ %) cases are near self-similarity further downstream. It is also interesting to note that for smaller x/D, the velocity profile decay with y approximately follows the envelope of the upstream flow (the free jet Gaussian-like profile). The velocity profiles between the screens are modulated by wakes from the screen rods, but the global behavior appears to follow remnants of the self-similarity Fig. 14b–d. This behavior persists for all x/D in the FOV for the larger ϕ (83.8 and 69 %), but for $\phi = 55.7$ %, the velocity profiles expand beyond the envelope of the upstream jet as x/D increases. In particular, at $x/D = 11.49$

(not shown), the jet profile has expanded across the entire channel containing the screens as the flow has decayed to very low velocities and has become nearly uniform across the flow domain.

Looking at the fine structure of the velocity profiles, Fig. 14 shows a decrease in thickness of the central, high velocity portion of the jets (i.e., the flow between the central screen rods) as ϕ decreases. From $x/D = 7.35$ to further downstream, this central portion of the flow shows nearly self-similar behavior for $\phi = 83.8$ and 69 %. The self-similarity is better for small e/D for higher ϕ screens (Musta 2012). Considering the $\phi = 55.7$ %, $e/D = 0.69$ case (Fig. 14d), it is worth noting that the large velocity peak surrounding the jet centerline persisted until $x/D = 11.49$. This may seem counter intuitive due to the expected higher dissipation for smaller e/D, but the smaller e/D constrains the central flow more severely, preserving the flow geometry in the central region by preventing mixing of the flow in between the screen planes, which also explains better the self-similarity for the low e/D cases. This was the case for all Reynolds numbers. The $\phi = 55.7$ % cases show nearly self-similar flow behavior for $x/D = 5.97$–10.11, where the velocity profiles are shifted up, showing higher dissipation and stronger spreading of the jet. Some asymmetry exists for the $e/D = 1.38$ case in the downstream region. The asymmetry in the downstream region for these cases is associated with the maximum velocity not appearing on the centerline (Fig. 14e). At these parts of the measurement domain for these test cases, the flow velocity was low and noise, pressure effects, or slight asymmetries in the screen array could lead to such shifts in the data.

The root-mean-squared (rms) magnitude of u' and v' were expressed dimensionlessly as $T_u = \frac{\sqrt{\langle u'^2 \rangle}}{U_{cl}}$ and $T_v = \frac{\sqrt{\langle v'^2 \rangle}}{U_{cl}}$ where $U_{cl} = U_{cl}(x)$. These turbulence intensity profiles are presented in Fig. 15 at $Re = 2000$ for $\phi = 100$ % and cases with screens for $\phi = 83.8$ and $\phi = 55.7$ % at $e/D = 0.69$. The $Re = 1000$ data are not presented here since these cases showed mainly steady laminar behavior, and the $\phi = 49.5$ % case was not considered here since its open area ratio is close to $\phi = 55.7$ % and the results were similar.

Overall the results show that for cases with screens the peak T_u increases with increasing ϕ, which is due to the localized nature of the screens when compared with the $\phi = 100$ % case (Fig. 15a–c). Additionally, nearly self-similar behavior can be observed for higher x/D's both for $\phi = 83.8$ %, $e/D = 0.69$ and for $\phi = 100$ %. The results for $\phi = 83.8$ % show that for $x/D < 7.35$ (upstream of the first screen) T_u has a peak value of 0.2–0.22 with a valley near the centerline (Fig. 15b). On the downstream of the first screen, the peak in T_u increases substantially. At $x/D = 9.44$ (downstream of the fourth screen), the profiles very nearly
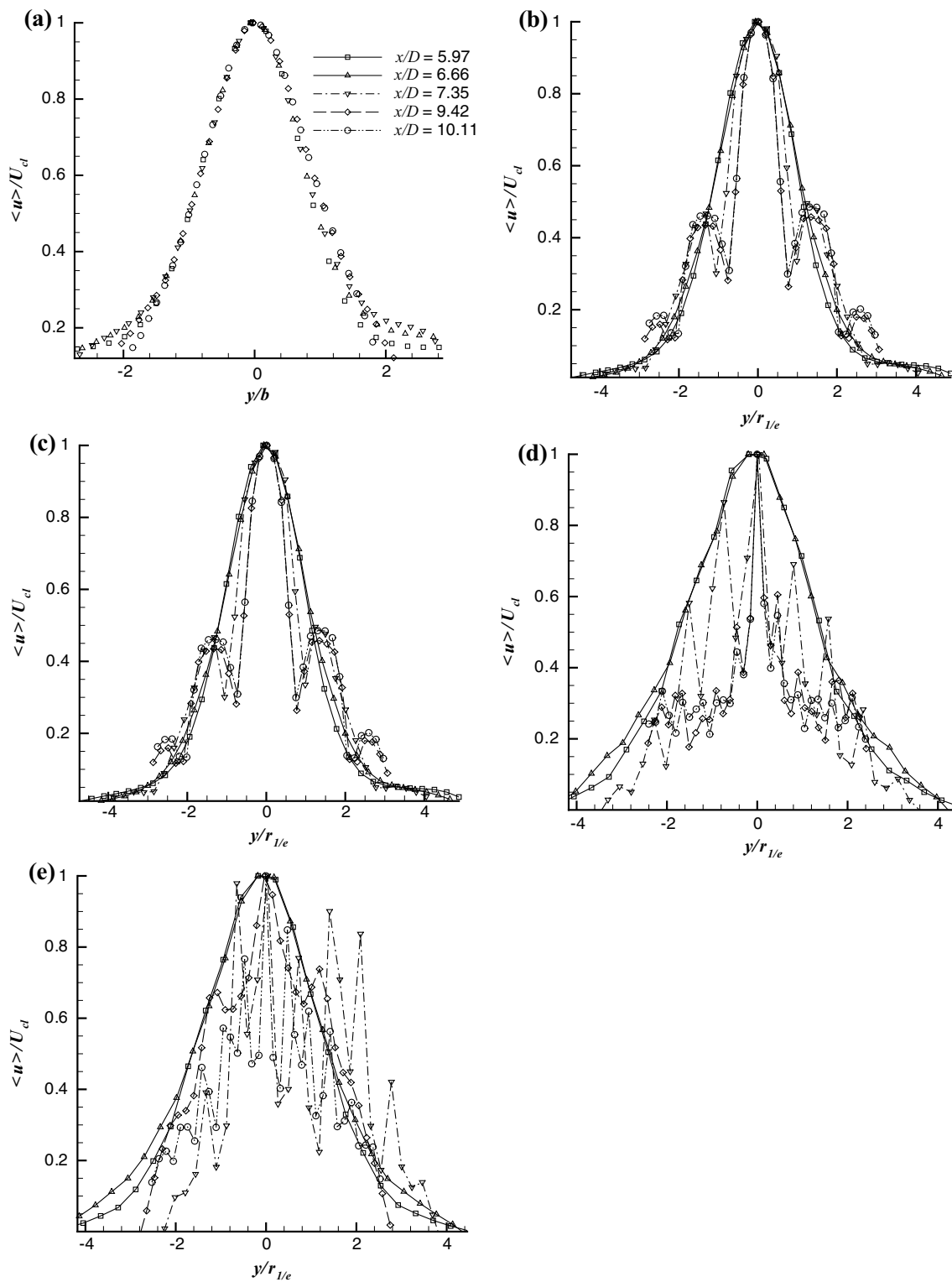
Fig. 14 Cross-sectional velocity profiles for $Re = 2000$: **a** $\phi = 100$ %; **b** $\phi = 83.8$ %, $e/D = 0.69$; **c** $\phi = 69.0$ %, $e/D = 0.69$; **d** $\phi = 55.7$ %, $e/D = 0.69$; and **e** $\phi = 55.7$ %, $e/D = 1.38$

collapse and the shape of the profile near the centerline has assumed the size of the center screen pore. The results for $\phi = 69.0$ % (not shown) are qualitatively similar.

The $\phi = 55.7$ % T_u results (Fig. 15c) give higher values than the larger ϕ cases (especially close to the first screen), which was due to the upstream unsteady jet motion through
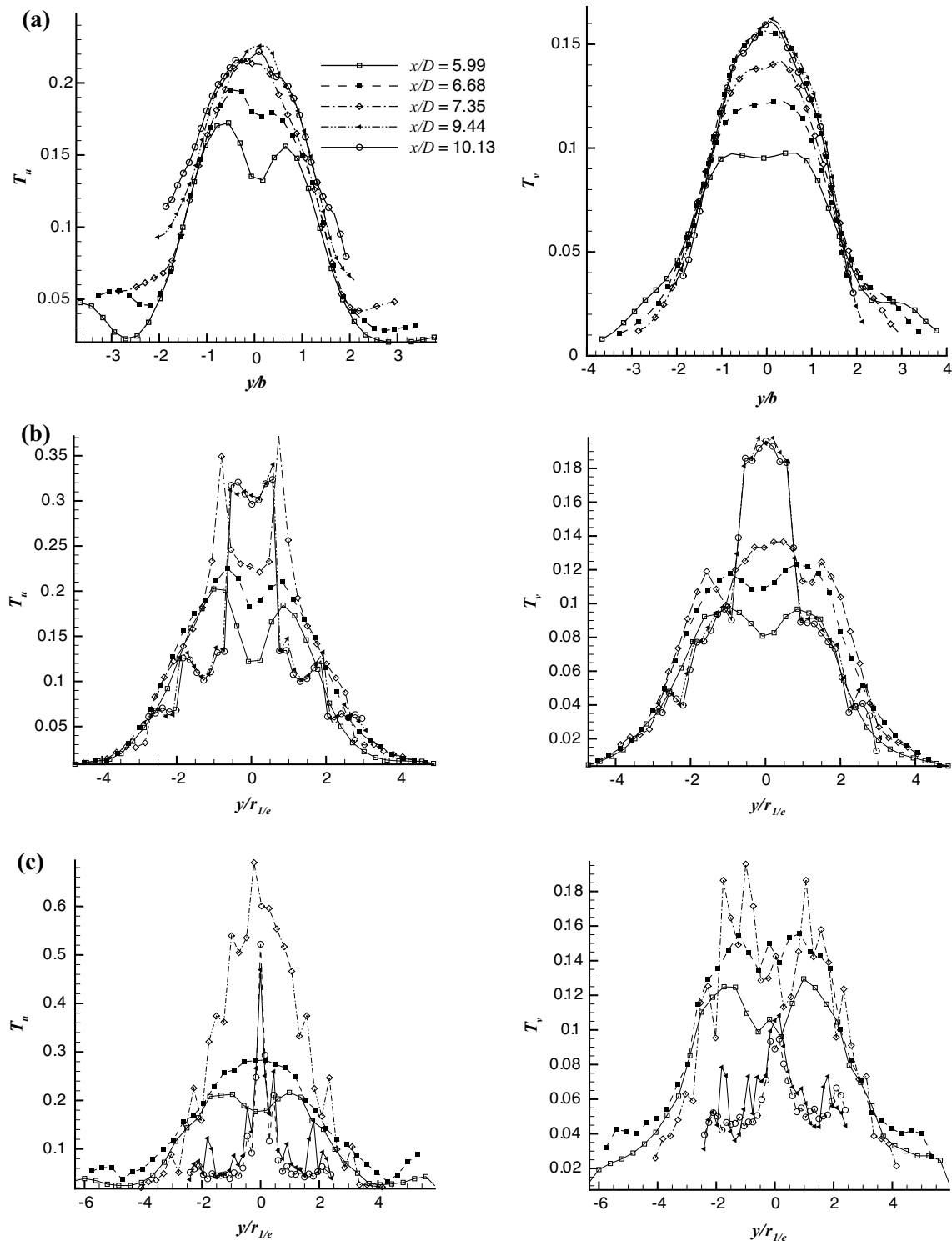
Fig. 15 T_u and T_v at $Re = 2000$. By Rows: **a** $\phi = 100$ %; **b** $\phi = 83.8$ %, $e/D = 0.69$; and **c** $\phi = 55.7$ %, $e/D = 0.69$

the screen as the jet was subjected to increased instability by the flow contraction through the screen pores where local velocity increased (Figs. 8, 9) and local maximum Reynolds number increased to as much as $Re = \frac{ue_r}{\nu} \approx 523$

and, based on the average velocity, $Re = \frac{\langle u \rangle e_r}{\nu} \approx 424$. At $x/D = 7.35$, there is a large peak on the centerline (a value of 0.7), which drops further downstream to 0.32. The overall shape for the large x/D is Gaussian-like, with
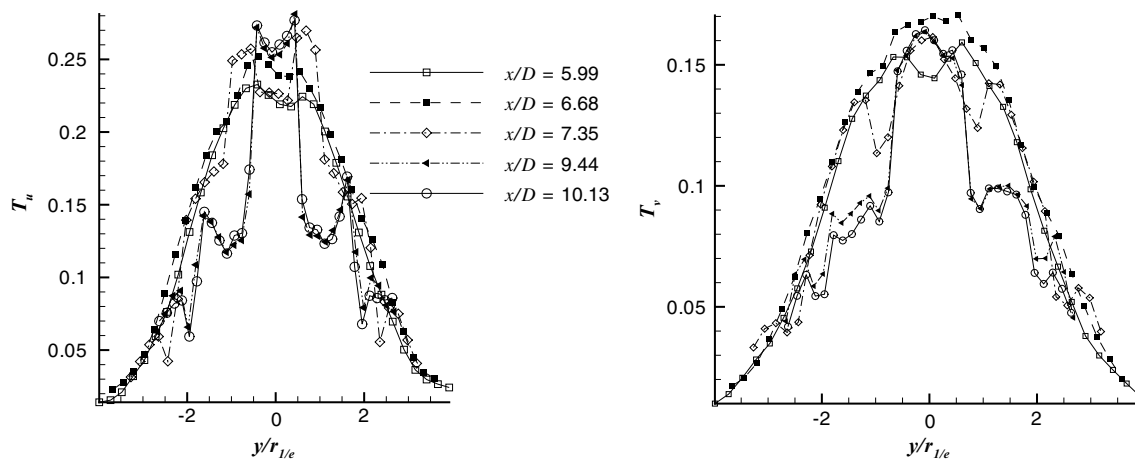
Fig. 16 T_u and T_v at $Re = 3000$: $\phi = 83.8$ %, $e/D = 0.69$

oscillations imposed by the screen rods. The final two axial locations have a sharp peak near the center and taper off smoothly for larger y without any oscillations on the plot. It should be noted that the downstream centerline velocities (i.e., denominators in T_u and T_v) are very low due to the high dissipation.

The effect of the Reynolds number on T_u can be analyzed by comparing Figs. 15 and 16 ($\phi = 83.8$ %). The results show a decrease in the peak T_u with higher Re. Except for data obtained at $x/D < 7.35$ (upstream of the first screen), the turbulence intensity profile shapes are similar for both Re at this ϕ. For $\phi < 83.8$ % at $Re = 3000$ (not shown here), the profile shapes are similar to $Re = 2000$, but T_u is generally larger at large $|y|$ and the peak values are lower (Musta 2012).

The T_v values are smaller than the T_u values at the same x/D for all cases and any increase in peak value after the first screen (if present) is smaller (Fig. 15a–c). For $Re = 2000$, the $\phi = 83.8$ % results are qualitatively similar to T_u, showing a double peak before the first screen, followed by an increase in the peak value further downstream with large values around the centerline in a region approximately the size of a screen pore, and self-similar behavior for $x/D \geq 9.42$ (downstream of the third screen). The results for $\phi = 69.0$ % (not shown) have similar behavior (Musta 2012). For $\phi = 55.7$ % and $x/D < 7.35$, the T_v are higher than larger ϕ cases, similar to the T_u data. For $x/D \geq 7.35$, there is a general increase in the T_v values, but without a strong peak on the centerline. For $x/D > 9.42$ (downstream of the fourth screen), there is a strong peak in the T_v profile on the centerline with a smooth and approximately monotonic decrease in value with increasing $|y|$. Increasing the Reynolds number to 3000 decreased the upstream peak values of T_v without a strong effect on the profile shape (except for $x/D = 7.35$, where the valley near the centerline

has essentially disappeared). For $x/D < 7.35$, the T_v values are generally similar to or smaller than the upstream peak values at $x/D = 6.68$.

Increasing e/D does not significantly affect the general shape of the T_u and T_v profiles, but changes with x/D are delayed to larger x/D since there are fewer screens.

Reynolds stress profiles, normalized by centerline velocity, are shown in Fig. 17 for $\phi = 100.0$ % and cases with screen for $\phi = 83.8$ and 55.7 % at $Re = 2000$. The $Re = 3000$ results show similar Reynolds stress profiles and are not shown here. The Reynolds stress profiles for the free jet (with the frame present) produced nearly self-similar profile shapes for $x/D > 6.66$ with peak Reynolds stress magnitude of ~0.015 (Fig. 17a). The cases with screens, on the other hand, have Reynolds stress profiles modulated by the screen geometry downstream of the first screen with self-similarity occurring only for large x/D at $\phi > 69.0$ %. Additionally, the peak values were increased over the free jet case by a factor of 2–3 after the first screen, and decreased well below the free jet values further downstream.

The Reynolds stress profiles for $\phi = 83.8$ % are nearly anti-symmetric with respect to the centerline ($y = 0$) for all x/D. At $x/D < 7.35$ (upstream of the first screen), the profile shape is similar to the free jet case where a sinus shape is expected (Fig. 17b). However, at $x/D \geq 7.35$, the profile contains two extrema on the positive and negative sides. The peak values on either side of the centerline continue to increase in magnitude with downstream location (the highest peak reaching a magnitude of approximately 0.032–0.033 near the centerline where the velocity is largest). The peak values remain approximately constant and the profile shape collapses to a nearly self-similar shape for $x/D \geq 9.44$.

The $\phi = 55.7$ %, $e/D = 0.69$ cases (Fig. 17c) have the highest peak for $x/D = 7.35$ downstream of the first screen. The number of extrema in the profile is larger for this case
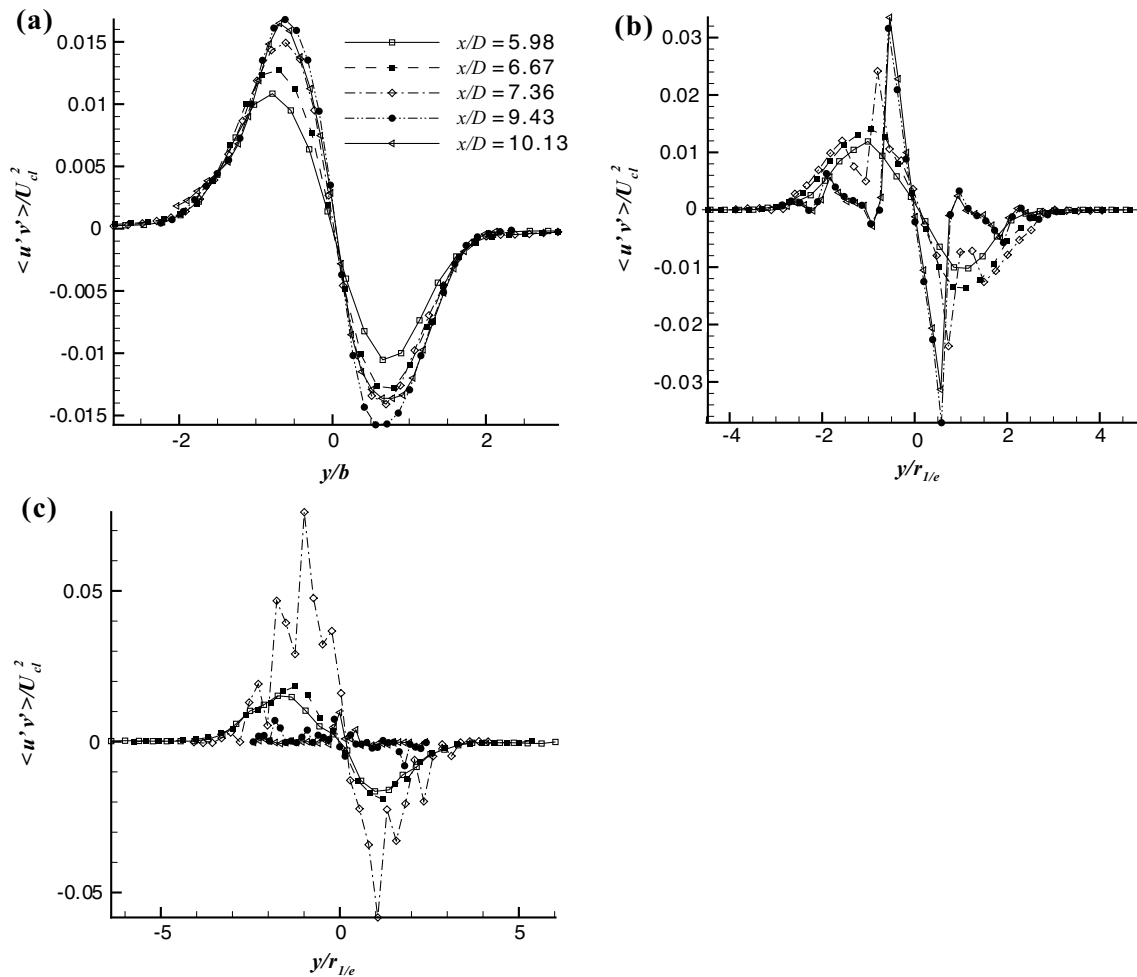
Fig. 17 Reynolds stress profiles at $Re = 2000$: **a** $\phi = 100.0\%$, **b** $\phi = 83.8\%$, $e/D = 0.69$; and **c** $\phi = 55.7\%$, $e/D = 0.69$

due to the increased number of screen rods, which generates multiple inter-pore "jets" between the screens for both cases. Increased corrugation of the profile is also seen for $\phi = 69.0\%$, $e/D = 0.69$ [not shown, see Musta (2012)]. For $x/D \geq 9.44$ (downstream of the second screen), there is decay of the Reynolds stress, especially away from the centerline. The data do not appear to collapse to a self-similar shape for the downstream range measured.

Increasing e/D gives a small decrease (~10 %) in the maximum Reynolds stresses amplitude for the $\phi = 83.8\%$ case and the profile shape remains similar. For the $\phi < 83.8\%$ cases, however, there is an increase of the maximum peak Reynolds stress amplitude (~49 % increase for $\phi = 69$ and ~110 % increase for $\phi = 55.7\%$) with a general overall increase in Reynolds stress magnitude compared to the lower e/D cases. This may be related to the mixing of the jet-like structures downstream of the screen rods (Musta 2012).

Increasing the Reynolds number to 3000 does not change the overall profile shape significantly, but it does generally increase the Reynolds stress values overall, except that the maximum magnitude of the Reynolds stress is reduced to ±0.02 for $\phi = 83.8\%$ and to ±0.045 for 55.7% (Musta 2012). At this Re, the $\phi = 83.8$–55.7% data for $e/D = 1.38$ do not show significantly higher peak values compared to the $e/D = 0.69$ results.

Total turbulent kinetic energy per unit mass is given by

$$\frac{E_{\text{turbk}}}{\rho} = \frac{1}{2}\left(\left\langle u'^2 \right\rangle + \left\langle v'^2 \right\rangle + \left\langle w'^2 \right\rangle\right) \tag{5.1}$$

For the present 2D results, the out-of-plane fluctuations were approximated by $\langle w'^2 \rangle \approx \langle v'^2 \rangle$, which was shown to be reasonable for axisymmetric free jets by Hussein et al. (1994). Figure 18 presents the total turbulent kinetic energy per unit mass, E_{turbk} (normalized by U_{jet}^2) for $\phi = 100, 83.8, 55.7,$ and 49.5%, $e/D = 0.69$–1.38, and $Re = 2000$. The $Re = 1000$ results are not shown because the flow is laminar and the kinetic energy from the fluctuations is generally low with the highest values downstream of the screen rods nearest the centerline, apparently
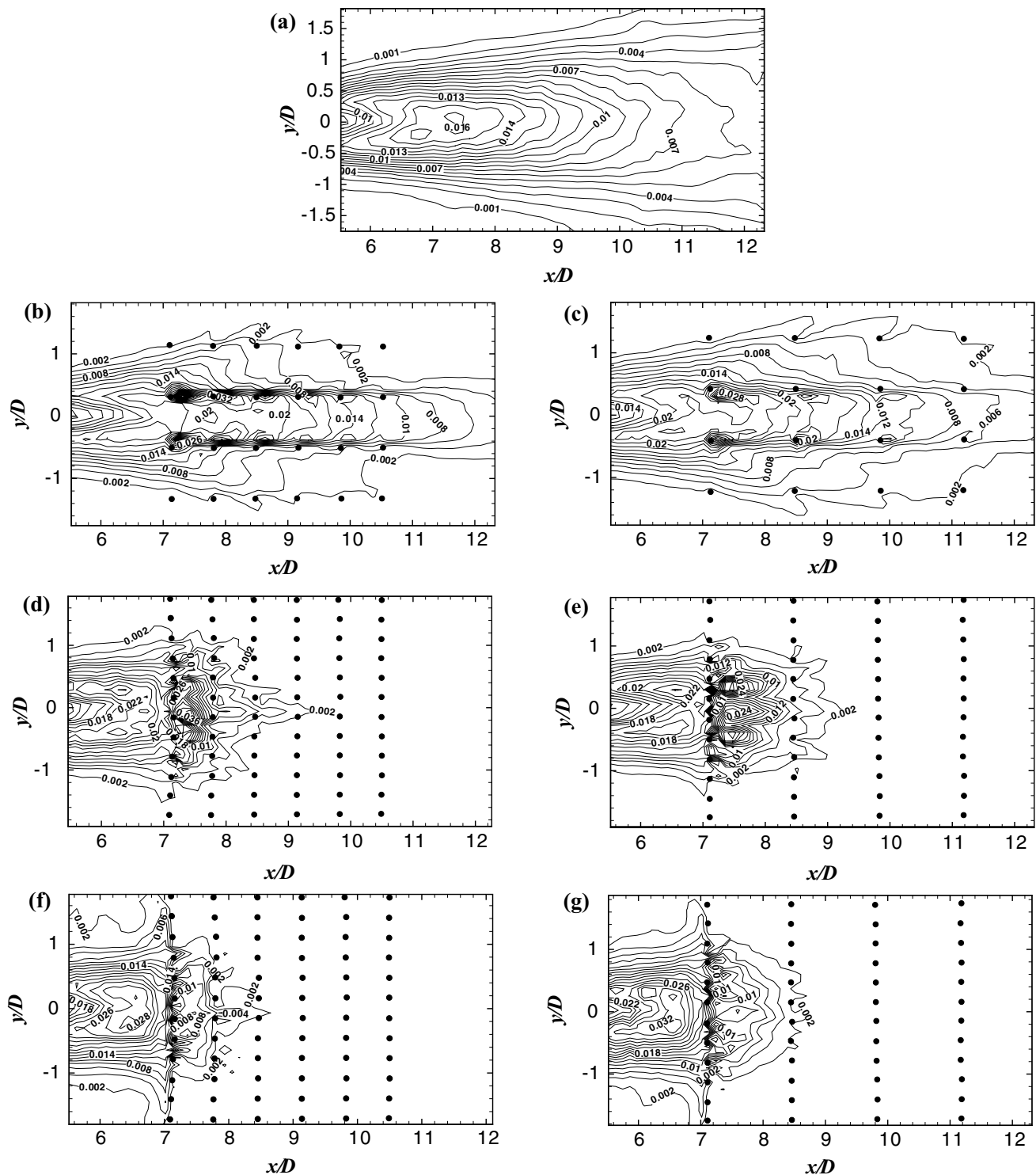
Fig. 18 Turbulent kinetic energy for $Re = 2000$: **a** $\phi = 100.0$ %, **b** $\phi = 83.8$ %, $e/D = 0.69$; **c** $\phi = 83.8$ %, $e/D = 1.38$; **d** $\phi = 55.7$ %, $e/D = 0.69$; **e** $\phi = 55.7$ %, $e/D = 1.38$; **f** $\phi = 49.5$ %, $e/D = 0.69$; and **g** $\phi = 49.5$ %, $e/D = 1.38$

introduced by the local flow separation around the screen rods. The $Re = 3000$ results are not shown because the turbulent kinetic energy profiles are similar to the $Re = 2000$ case (Musta 2012).

In Fig. 18, the overall magnitude and extent of E_{turbk} are larger for $\phi = 100$ %, which is expected since the flow was unsteady and no longer completely laminar for this case. For $\phi < 100$ %, the peak E_{turbk} increased dramatically,

with large local E_{turbk} values downstream of the screens rods, except for $\phi = 49.5$ % which shows very rapid dissipation downstream of the first screen (Fig. 18f–g). For higher ϕ values [$\phi > 55.7$ %, including $\phi = 69.0$ % (not shown)], increasing the number of screens (decreasing e/D) tended to increase length of elevated E_{turbk}, but the overall maximum turbulent kinetic energy (located behind the first screen) stayed almost same between the two e/D cases. For lower ϕ, where the screens provide more dissipation, increasing e/D increased the turbulent kinetic energy between screen rods. Increasing Re to 3000 showed limited effect, but did increase the relative magnitude of the turbulent kinetic energy downstream of the first screen for $\phi = 49.5$ % (Musta 2012).

6 Jet momentum flux

Momentum flux of the jet is a key metric for jet flows interacting with permeable screens because for free jets this quantity is conserved in the axial direction (Capp 1983; Webb and Castro 2006). For the present investigation, however, drag from the screens removes momentum from the flow, which reduces the momentum flux from the jet and provides an important metric of the effect of the screens on the flow. The time-averaged jet momentum flux with the contribution of an axial pressure gradient for an axisymmetric jet flow is given by

$$M(x) = \int_{0}^{H/2} 2\pi\rho y \left\{ \langle u \rangle^2 + \left\langle u'^2 \right\rangle - \frac{\left\langle v'^2 \right\rangle + \left\langle w'^2 \right\rangle}{2} \right\} \mathrm{d}y \tag{6.1}$$

where u is the axial velocity, and u', v', and w' are fluctuating components in axial, radial, and azimuthal directions, respectively (George 1990; and Hussein et al. 1994). An axial pressure gradient across the jet in this equation appears as the radial and azimuthal fluctuating velocity components and was derived from the radial momentum equation for the jet. The fluctuations were calculated from the DPIV data as $u' = u - \langle u \rangle$ and $v' = v - \langle v \rangle$. The same approximation used in the kinetic energy results was used here for the out-of-plane velocity fluctuations, in which case Eq. 6.1 reduces to

$$M(x) = \int_{0}^{H/2} 2\pi\rho y \left\{ \langle u \rangle^2 + \left\langle u'^2 \right\rangle - \left\langle v'^2 \right\rangle \right\} \mathrm{d}y \tag{6.2}$$

Equations (6.1) and (6.2) assume axisymmetry of the flow at every downstream location in order to complete the integration in the azimuthal direction (using profiles measured in the x–y plane). While the grid geometry of the screens used in this investigation (Fig. 3) prevents perfect axisymmetry, approximate axisymmetry in an average sense is expected (i.e., the flow variations along lines through the origin in the y–z plane are similar on average), which is also supported from the y–z mean velocity profiles in Fig. 10. In particular, Eqs. (6.1) and (6.2) properly weight the flow at larger y more heavily because of the greater associated flux area. Additionally, calculations of $M(x)$ from both positive and negative y were averaged to help account for asymmetries in the flow. The lack of true flow axisymmetry, however, limits the accuracy of Eqs. (6.1) and (6.2) somewhat for the present results (for example in determining the drag force on each screen). Nevertheless, as the dominant physics are captured by these equations, they can be expected to reliably determine the trends in momentum flux for purposes of comparison between cases investigated herein (though perhaps not with results for different configurations) because errors in the calculation are expected to be similar between cases.

The momentum flux results from Eq. (6.2) are shown in Fig. 19 for all cases considered. In this figure, the momentum flux was normalized by the initial upstream value at $x/D = 5.84$ (M_0). The momentum flux was computed between the screens at the same axial locations for all cases. This was done to avoid variations of the flow associated with the slowing and acceleration of the flow as it approached and passed through the screens due to the local pressure variation around the screens.

For $Re = 1000$, the free jet results ($\phi = 100$ %) with and without the frame present are similar and show very little change with x, which is expected since the jet diameter is small and the flow should not be strongly affected by the frame. The higher Reynolds number free jet results show a bump at intermediate x/D for the cases with the frame present. Capp (1983) discussed confinement effects and indicated that for insufficiently large jet facilities at high Reynolds numbers, returned flow (recirculation) of the entrainment regions leads to momentum loss. To prevent this, the flow facility should be more than the 10^5 times that of the jet exit area (Capp 1983). The effect of confinement was verified by the work of Hussein et al. (1994). Although the present study can be considered a confined jet ($\frac{A_{\mathrm{frame}}}{A_{\mathrm{jet}}} = 2055 \pm 2$) for $x/D > 5.7$, no observable return flow was detected in the instantaneous or time-averaged velocity fields (Musta 2012). However, due to the confined environment, the effect of the frame wall was still detected in M.

For cases with screens, the change in M with x in Fig. 19 shows that the momentum removal increases with decreasing ϕ and increasing Reynolds number, as expected. Additionally, e/D has a significant effect on M, with M decreasing more rapidly for smaller e/D because momentum is removed more frequently in x for these cases. For lower ϕ values ($\phi < 69.0$ %), the e/D effect is not as distinctive since most of the momentum is extracted by the first screen and the highest decay of the momentum flux is for the
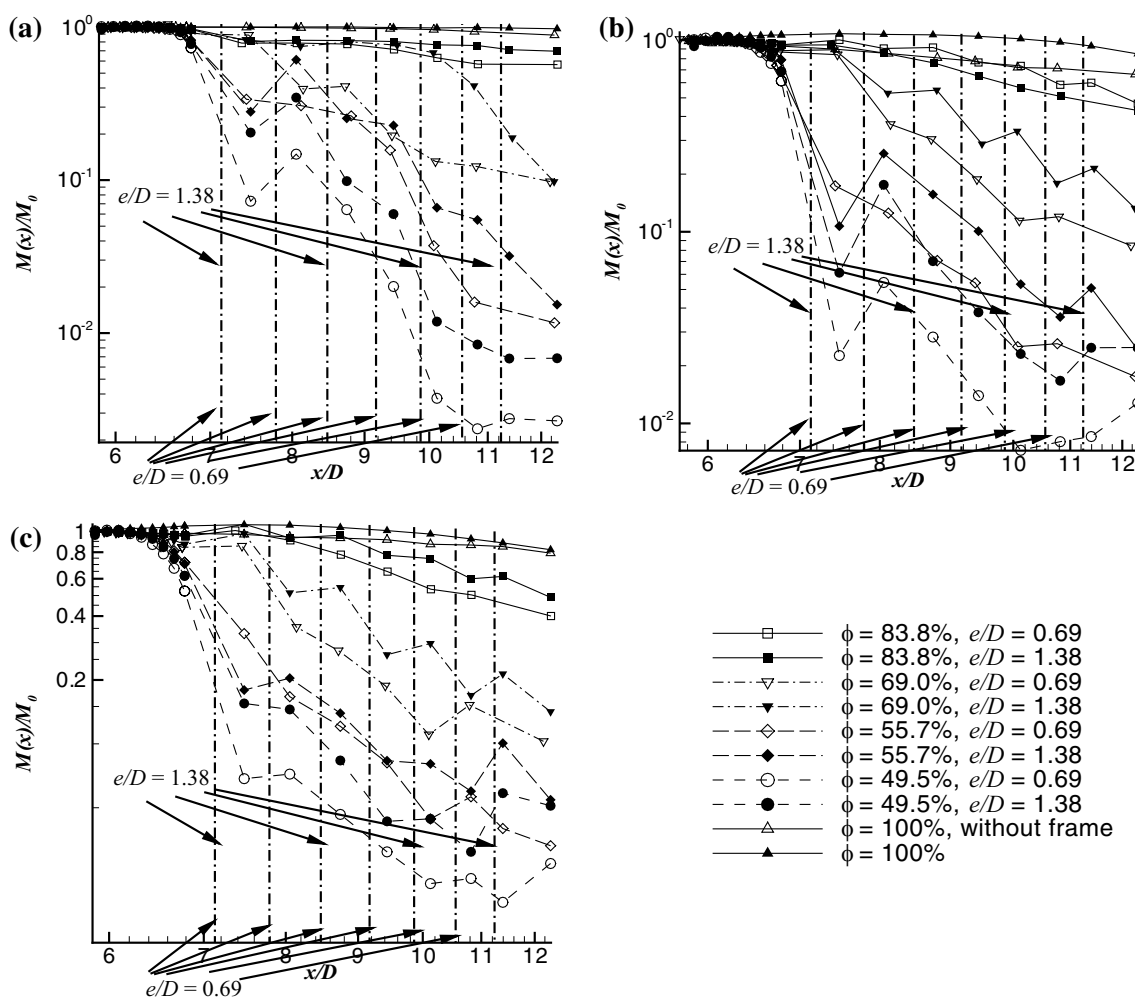
Fig. 19 Momentum flux for **a** $Re = 1000$, **b** $Re = 2000$, and **c** $Re = 3000$

$\phi = 49.5\%$ screens. For similar reasons, the effect of e/D is diminished for $Re = 3000$.

7 Discussion

Comparing the effect of Re on the qualitative flow behavior showed a dramatic shift in the flow evolution as Re increased above 1000. For $Re = 1000$, impingement of the flow on the porous screens produced large wake regions behind the screen rods because the local flow Re was large enough to effect flow separation around the screens. The Re was not so high, however, that the resulting separated jets became transitional or turbulent (they remained almost entirely steady as discussed previously), so the entrainment rate of the separated jets remained low, preventing the wakes from closing a short distance behind the screen rods. For higher Re, the flow had an unsteady and turbulent character (see, for example, the $Re = 3000$ results)

which caused the flow to fill in downstream of the screens. The screens affected the spreading rate and momentum and energy decay, but the mean flow direction was affected much less strongly by the local screen features for $Re > 1000$.

Inside the permeable screens, self-similarity was observed for cross-sectional mean velocity profiles (for $\phi > 55.7\%$) and some turbulent quantities (e.g., Reynolds stress for $\phi > 69.0\%$) in the $Re > 1000$ cases. This may be somewhat unexpected given the very segregated nature of the flow observed at $Re = 1000$. The structure of the permeable screens likely played a role in this behavior. The screens comprised a regular series of grids, and the flow tended to be directed through the voids/pores in the screens to form smaller jets. Because the screen geometry was aligned, these smaller jets could persist through several screens so that each "pore jet" would be able to achieve local self-similarity. Likewise, the persistence of the central pore jet was related to the regular screen structure. The

central pore jet persisted longer than the flow at larger y/D because the flow near the centerline was aligned with the screen geometry (flow at larger y/D had a remnant v component), so it was not dissipated as strongly by the screens. If the screens do not have a regular, aligned grid pattern throughout, the local self-similarity of flow through pores would not be expected, but the self-similarity of the overall jet flow would be likely to persist over some region of the porous domain if Re was sufficiently high.

Investigation on the effect of Re number was limited due to experimental capabilities of the present investigation. For $Re > 10^4$, enhanced mixing downstream of the screen rods would be expected due to the expected higher turbulence levels on the upstream side of the first screen and higher Re_d. In addition, deeper penetration of the flow through the screens would be expected, along with smaller-scale structures between the screens. However, the qualitative observations about the self-similar behavior of the results and decay rates (for energy, centerline velocity, etc.) are expected to remain as they showed little Re dependence over the limited range investigated. Additional experimental study for higher Re would nevertheless be useful for understanding applications involving higher Re.

8 Conclusions

The effect of permeable screens on the intermediate region of steady jets was studied in terms of centerline velocity decay, evolution of the jet half-width, profiles of velocity and Reynolds stress tensor components, and momentum flux for $Re = 1000$–3000. The results showed laminar, predominantly steady flow behavior for $Re = 1000$. For this Re, the flow became segregated inside the porous domain, with large wakes regions, which was very dissimilar from jet behavior in a clear fluid. For $Re \geq 2000$, the jet showed unsteady and turbulent behavior with a more smoothly distributed mean flow field inside the porous domain. As a result, more traditional jet features of self-similarity and increasing jet width were compared for the higher Reynolds number cases. Jet penetration along the centerline was significant (and related to the regular structure of the screens), with strong decay along the lateral (y) axis. Decreasing ϕ significantly increased the jet width and the rate of increase of the jet width compared to the free jet case. Additionally, the jet centerline velocity was significantly decreased and its decay rate was significantly increased by decreasing ϕ. Self-similarity (or near self-similar behavior) was observed in the downstream flow field at $\phi = 83.8$ and 69.0 % for the cross-sectional profiles of velocity, Reynolds stress, and turbulence intensity, but the shape of the profiles seemed to be locked to the grid structure. Changes in the cross-sectional turbulence intensity and Reynolds stress were affected mostly by ϕ rather than Re or the screen spacing. The peak values in turbulence intensity and Reynolds stress tended to increase as ϕ decreased, but decreased sharply downstream of the first screen. Turbulent kinetic energy showed large values concentrated downstream of the screen rods. For the $\phi > 55.7$ % cases, the turbulent kinetic energy was distributed downstream through the porous domain, whereas for the $\phi < 69$ % cases (high dissipation), the turbulent kinetic energy was confined to a small region downstream of the first screen. The screens' extracted momentum from the jet at a higher rate for lower ϕ and the effect of e/D was significant for the higher ϕ values. M decreased more rapidly for smaller e/D because momentum was removed more frequently in x for these cases.

References

Cant R, Castro I, Walklate P (2002) Plane jets impinging on porous walls. Exp Fluids 32:16–26

Capp SP (1983) 'Experimental Investigation of the Turbulent Axisymmetric Jet', PhD Dissertation. Dept Mech and Aero Engineering, University of Buffalo, SUNNY

Crow S, Champagne F (1971) Orderly structure in jet turbulence. J Fluid Mech 48:547–591

Fu WS, Huang H-C (1997) Thermal performance of different shape porous blocks under an impinging jet. Int J Heat Mass Transf 40(10):2261–2272

George WK (1990) Governing equations, experiments and the experimentalist. Exp Therm Fluid Sci 3:557–566

Graminho DR, Lemos MJ (2009) Simulation of turbulent impinging jet into a cylindrical chamber with and without a porous layer at the bottom. Int J Heat Mass Transf 52(3):680–693

Hussein HJ, Capp SP, George WK (1994) Velocity measurements in a high-Reynolds-number, momentum-conserving, axisymmetric, turbulent jet. J Fluid Mech 258:31–75

Jeng T-M, Tzeng S-C (2005) Numerical study of confined slot jet impinging on porous metallic foam heat sink. Int J Heat Mass Transf 48(23):4685–4694

Jugjai S, Wongpanit N, Laokethan T, Nokkaew S (2002) The combustion of liquid fuels using a porous medium. Exp Therm Fluid Sci 26(1):15–23

Kudra T, Mujumdar AS (2009) Advanced drying technologies. CRC Press, Taylor & Francis Group, US

Kwon S, Seo IW (2005) Reynolds number effects on the behavior of a non-buoyant round jet. Exp Fluids 38:801–812

Moreira RG (2001) Impingement drying of foods using hot air and superheated steam. J Food Eng 49:291–295

Musta MN (2012) Interaction of steady jets and vortex rings with an array of multible permeable screens Ph.D. Thesis, Southern Methodist University

Musta MN, Krueger PS (2014) Interaction of vortex rings with multiple permeable secreens. Phys Fluids 26:113101

Pedocchi F, Martin JE, Garcia MH (2008) Inexpensive fluorescent particles for large-scale experiments using particle image velocimetry. Exp Fluids 45:183–386

Prakash M, Turan OF, Li Y, Mahoney J, Thorpea GR (2001a) Impinging round jet studies in a cylindrical enclosure with and without

a porous layer: part I: flow visualizations and simulations. Chem Eng Sci 56:3855–3878

Prakash M, Turan OF, Li Y, Mahoney J, Thorpea GR (2001b) Impinging round jet studies in a cylindrical enclosure with and without a porous layer: part II: LDV measurements and simulations. Chem Eng Sci 56:3879–3892

Shahangian N, Ghojel J (2010) Investigation of the interaction between diesel spray and porous medium. In: 17th Australasian fluid mechanics conference. Australasian Fluid Mechanics Conference, Auckland, New Zealand

Todde V, Spazzini PG, Sandberg M (2009) Experimental analysis of low Reynolds number free jets evolution along the jet centerline and Reynolds number effects. Exp Fluids 47:279–294

Uzol O, Chow YC, Katz J, Meneveau C (2002) Unobstructed particle image velocimetry measurements within an axial turbo-pump using liquid and blades with matched refractive indices. Exp Fluids 33:909–919

Webb S, Castro IP (2006) Axisymmetric jets impinging on porous walls. Exp Fluids 40:951–961

Westerweel J, Dabiri D, Gharib M (1997) The effect of a discrete window offset on the accuracy of cross-correlation analysis of digital PIV recordings. Exp Fluids 23:20–28

Willert CE, Gharib M (1991) Digital particle image velocimetry. Exp Fluids 10:181–193

Wilson BM, Smith BL (2013) Uncertainty on PIV mean and fluctuating velocity due to bias and random errors. Meas Sci Technol 24:035302